Assessing Hurricane Rainfall Mechanisms Using a Physics-Based Model: Hurricanes Isabel (2003) and Irene (2011)

PING LU AND NING LIN

Department of Civil and Environmental Engineering, Princeton University, Princeton, New Jersey

KERRY EMANUEL

Department of Earth, Atmospheric and Planetary Sciences, Massachusetts Institute of Technology, Cambridge, Massachusetts

DANIEL CHAVAS

Department of Earth, Atmospheric, and Planetary Sciences, Purdue University, West Lafayette, Indiana

JAMES SMITH

Department of Civil and Environmental Engineering, Princeton University, Princeton, New Jersey

(Manuscript received 7 September 2017, in final form 6 February 2018)

ABSTRACT

We examine a recently developed physics-based tropical cyclone rainfall (TCR) model and apply it to assess the mechanisms that dominate the magnitude and spatial distribution of TC rainfall, with Hurricanes Isabel (2003) and Irene (2011) as study cases. We evaluate the TCR model using Weather and Research Forecasting (WRF) Model simulations. TCR-generated rainfall fields for the two storms compare well with WRF estimates in terms of both azimuthal mean and spatial distributions. When coupled with a hydrologic model, TCR generates flood peaks over the Delaware River basin for Irene as accurately as WRF. TCR accounts for four major rainfall mechanisms: surface frictional convergence, vortex stretching, interaction of the storm with topography, and interaction of the storm with large-scale baroclinity. We show that these rainfall mechanisms affected the rainfall pattern differently for Isabel and Irene. Frictional convergence is the dominant factor, while other mechanisms are also significant. The frictional convergence depends on the boundary layer formulation, which is relatively simple in TCR and may require calibration of boundary layer parameters. Furthermore, we find that the TC rainfall distribution is strongly dependent on the temporal and spatial variation of the TC wind field, mediated by the physical mechanisms represented by TCR. When coupled with various analytical wind models, TCR generally captures the rainfall distribution, with the Holland wind model performing the best. Given its high computational efficiency, TCR can be coupled with an analytical wind model, a hydrological model, and a TC climatology model to generate large numbers of synthetic events to assess the risk associated with TC rainfall and inland flooding.

1. Introduction

Rainfall and freshwater flooding from tropical cyclones (TCs) have caused large numbers of fatalities and vast economic damage (Rappaport 2000, 2014; Czajkowski et al. 2011, 2013, 2017; Rezapour and Baldock 2014), and they have been shown to play an important role in controlling the upper tail of flood distributions in the eastern United States (Smith et al. 2011; Villarini and Smith 2010). Moreover, TC rainfall may significantly increase in the future due to likely increases of atmospheric moisture content and potential changes of storm activity (Knutson and Tuleya 2004; Knutson et al. 2010, 2013; Villarini et al. 2014a; Emanuel 2013). Compared to other TC hazards such as severe wind and storm surge (e.g., Chavas et al. 2015, hereafter C15; Dietrich et al. 2010; Lin and Emanuel 2016), TC rainfall and induced freshwater flooding are less well understood (Elsberry 2002; Villarini et al. 2014b). Advancing the understanding,

Denotes content that is immediately available upon publication as open access.

Corresponding author: Ping Lu, luping53@gmail.com

DOI: 10.1175/JAS-D-17-0264.1

modeling, and risk assessment of TC rainfall is therefore an important task.

Water plays an essential role in TCs; evaporation of seawater into the air is the most important source of energy driving TCs (Emanuel 1986, 1991). TCs typically form from cloud clusters over large bodies of warm water. The inflowing air toward the low-pressure center experiences a large increase in entropy owing to surface enthalpy fluxes. Air then rises nearly moist adiabatically in the eyewall and eventually loses its excess entropy by exporting it at the very low temperatures of the tropical tropopause layer. This flow of heat constitutes a Carnot engine, with the surface enthalpy flux acting as the heat source and with a thermodynamic efficiency proportional to the difference between the surface and tropopause temperatures. As TCs make landfall, increased friction over the land surface enhances the convergence of air (Ekman pumping), resulting initially in increased rainfall. At the same time, TCs are cut off from their oceanic energy source and dissipate quickly.

By its nature, TC rainfall is closely related to storm intensity and intensification, and it varies with radius from the storm center (Lonfat et al. 2004). The movement of the storm and its interaction with the environment, such as topography (Smith 2006; Cheung et al. 2008; Yang et al. 2011), large-scale baroclinity/vertical wind shear (Rogers et al. 2003; Wong and Chan 2004; Chen et al. 2006), and extratropical systems (Harr and Elsberry 2000; Harr et al. 2000; Jones et al. 2003; Atallah and Bosart 2003), can greatly affect the storm structure and convection, resulting in often highly asymmetric rainfall distributions.

Despite the understanding of basic TC rainfall characteristics, the literature on TC rainfall modeling is limited (Rogers et al. 2009). Before the era of remote sensing, researchers relied on sparse rain gauge observations to estimate TC rainfall (Riehl and Malkus 1961; Simpson and Riehl 1981). With the development of radar and satellite observations providing vast amounts of TC rainfall data, it became possible to conduct systematic analyses. Statistical methods including the rainfall climatology and persistence (R-CLIPER) model (Lonfat et al. 2004; Tuleya et al. 2007) and the parametric hurricane rainfall model (PHRaM; Lonfat et al. 2007) were thus developed based on rainfall data from the Tropical Rainfall Measuring Mission (TRMM) and used operationally by the National Hurricane Center for TC rainfall forecasting. R-CLIPER estimates the mean amplitude of rainfall as a function of storm radius and wind intensity. Building on R-CLIPER, PHRaM incorporates rainfall asymmetry by adding an azimuthal Fourier decomposition to account for the effect of shear and a low-level flow-dependent gradient of ground elevation to account for the effect of topography. Because of the ensemble-averaging nature, however, the dependence of rainfall on storm characteristics is coarse in these statistical models, and rainfall extremes are often not captured (Tuleya et al. 2007; Langousis and Veneziano 2009a; Mudd et al. 2015).

Besides the statistical approach, Langousis and Veneziano (2009a) developed the modified Smith for rainfall (MSR) model, based on basic thermodynamics and TC boundary layer theory (Langousis et al. 2008). Evaluated with the case study of Hurricane Frances (2004) using high-resolution numerical model (MM5) simulations and TRMM measurements, MSR was shown to produce significantly improved azimuthal rainfall estimates compared to R-CLIPER (Langousis and Veneziano 2009a). Explicitly modeling the rainfall induced by horizontal wind convergence in the boundary layer, MSR accounts for the azimuthal asymmetries in surface friction related to storm motion, but it does not account for the interaction of the storm with its environment (wind shear, topography, etc.) and is applicable only for open-water or near-water sites.

In this paper, we review and investigate a physics-based TC rainfall (TCR) model, which gives spatial rainfall estimates along the storm track (over open water and land). The rainfall is related to upward vapor flux, which is contributed by frictional convergence (Ekman pumping), changes in the axisymmetric vorticity of the gradient wind (vortex spinup and spindown), and interaction of the storm with topography and large-scale baroclinity (wind shear). TCR employs the radial profile of the gradient wind, storm translation, and surface roughness to estimate the effect of frictional convergence, similar to MSR but with a simplified parameterization. The interaction of the storm with large-scale baroclinity is accounted for by incorporating the wind shear directly. The interaction of the storm with topography is accounted for through incorporating ground elevation, similar to PHRaM. Unlike all the models discussed above, TCR also considers the effect of storm intensification and weakening associated with vortex spinup and spindown. In addition, TCR is phrased in a clear physics-based framework, with only a limited number of input parameters that may be calibrated with observations, making it a convenient tool for investigating the different rainfall mechanisms (i.e., effects of storm characteristics and the large-scale environment such as topography and wind shear).

TCR was initially developed as part of a synthetic approach for estimating TC hazard (Emanuel et al. 2008). Zhu et al. (2013) first described the rainfall algorithm and investigated the model's ability to capture the overall statistics of TC rainfall. They applied the TC

rainfall hazard model to Texas and found that the synthetic TC rainfall climatology agrees well with TC rainfall return periods calculated from rain gauge observations. Emanuel (2017) used the TC rainfall hazard model to assess the present and future probability of Hurricane Harvey's (2017) rainfall. In this study, we examine TCR on an event basis and apply it to investigate major rainfall mechanisms for two extreme cases: Hurricanes Isabel (2003) and Irene (2011). First, we evaluate TCR with a high-resolution numerical model, the Weather Research and Forecasting (WRF) Model (Davis et al. 2008). With WRF-generated storm wind characteristics and environment as input for TCR, the WRF- and TCR-generated rainfall fields are compared. In addition, riverine floods induced by Hurricane Irene over the Delaware River basin are estimated by coupling TCR and WRF with a hydrological model, and the estimated flood magnitudes are compared with gauge observations. Next, given its advantage of explicitly modeling the different rainfall mechanisms discussed above, we apply TCR to examine these rainfall mechanisms for Hurricanes Isabel and Irene. Then, to facilitate the application of TCR, we evaluate the performance of TCR when coupled with analytical wind models. We also explore the sensitivity of TCR to other modeling parameters such as the drag coefficient.

This paper is organized as follows. In section 2, we review TCR by summarizing its formulation. In section 3, we compare TCR with WRF in terms of generated azimuthal mean and spatial rainfall distributions as well as riverine flood peaks. In section 4, we examine the components of TCR and investigate the different rainfall mechanisms. In section 5, we investigate the performance of TCR when coupled with analytical wind models and conduct sensitivity analyses. In section 6, we summarize major findings of this study.

2. TCR model

The main components of TCR were introduced and discussed briefly by Zhu et al. (2013). Here we present the model in more detail, explaining its formulation and parameters. TCR is a horizontally distributed and vertically integrated model, where rainfall is estimated by upward vapor flux wq_s. Let P_{rate} be the precipitation rate:

$$P_{\text{rate}} = \epsilon_p \frac{\rho_{\text{air}}}{\rho_{\text{liquid}}} q_s w, \quad (\text{when} \quad w > 0), \tag{1}$$

where ϵ_p is precipitation efficiency; ρ_{air} and ρ_{liquid} are the density of water vapor and liquid water, respectively (the ratio is set to 0.0012); q_s is saturation specific humidity; and w is the vertical velocity. Previous studies have related upward vapor flux to rainfall (Alpert 1986; Magagi and Barros 2004; Wilson and Toumi 2005; Langousis and Veneziano 2009a), and we discuss in detail this P_{rate}–wq_s relationship in section 4. The core of TCR is the estimation of the vertical velocity w, which is deduced from the time-evolving, axisymmetric storm wind field and the environmental winds, as follows.

We begin by estimating the vertical velocity at the top of the frictional inflow layer in a circular vortex. We assume that in this layer, the principal balance is between radial advection of angular momentum and frictional torque acting on the azimuthal velocity (Ooyama 1969; Kepert 2001, 2013):

$$u\frac{\partial M}{\partial r} \simeq -r\frac{\partial \tau_\theta}{\partial z}, \tag{2}$$

where u is the radial velocity, r is the radius from the storm center, M is the absolute angular momentum per unit mass [$M = rV + (1/2)fV^2$, where V is the azimuthal wind speed and f is the Coriolis parameter], and τ_θ is the azimuthal turbulent stress.

Assuming incompressible flow, the equation of mass continuity may be written

$$\frac{\partial w}{\partial z} = -\frac{1}{r}\frac{\partial}{\partial r}(ru), \tag{3}$$

where w is the vertical velocity. Substituting (2) into (3) yields

$$\frac{\partial w}{\partial z} = \frac{1}{r}\frac{\partial}{\partial r}\left(r^2 \frac{\partial \tau_\theta/\partial z}{\partial M/\partial r}\right). \tag{4}$$

If we assume that M does not vary much with altitude within the boundary layer, then (4) may be integrated vertically through the depth of the boundary layer to give the vertical velocity at the top of the boundary w_b:

$$w_b = w_h + w_f, \tag{5}$$

where

$$w_f \equiv -\frac{1}{r}\frac{\partial}{\partial r}\left(r^2 \frac{\tau_{\theta s}}{\partial M/\partial r}\right), \tag{6}$$

where $\tau_{\theta s}$ is the azimuthal surface stress and w_h is the surface vertical velocity, which we take as the topographically induced motion:

$$w_h = \mathbf{V} \cdot \nabla h, \tag{7}$$

where h is the topographic height and $\mathbf{V}$ is the horizontal wind velocity, given as the vector sum of the storm

gradient wind (here, we ignore the radial component of storm flow) and the environmental background wind. This approximation crudely accounts for the strong dependence of topographically induced rainfall on the interaction of surface wind and terrain gradients. More sophisticated orographic precipitation models also account for the effects of stratification and cloud microphysics (Barstad and Smith 2005). In addition, to avoid nonphysical rainfall in the storm periphery over mountainous regions, this topography effect is reduced outside the storm center. In the original algorithm used in Zhu et al. (2013) and Emanuel (2017), this topography effect is reduced according to the distance from the storm center. Here we simply set w_h to be zero, when $|\mathbf{V}|$ is smaller than a threshold (V_{th}; see section 5 for details).

We model the surface stress as

$$\tau_{\theta s} = -C_d|\mathbf{V}|V, \tag{8}$$

where C_d is the (possibly wind dependent) drag coefficient, and $|\mathbf{V}|$ is the absolute value of the total surface wind, including the storm's azimuthal wind and the environmental wind. Since $|\mathbf{V}|$ is not, in general, axisymmetric, neither will be the vertical motion at the top of the boundary layer (we note, however, that the asymmetry induced by the convergence of the azimuthal wind due to the spatial variation of C_d is neglected). As pointed out by Ooyama (1969) and Kepert (2013), here C_d should be reduced from its usual value, since the surface stress is calculated from the gradient wind (close to boundary layer mean), rather than the 10-m wind. Also, C_d may be applied as a function of wind (over ocean) and/or of ground elevation [over land; as in the original algorithm used in Zhu et al. (2013) and Emanuel (2017)], but here we simply treat C_d as different constants for ocean and land (model sensitivity to C_d is discussed in section 5).

The next component of the vertical velocity is that associated with changes in the storm's vorticity (vortex stretching). Since the low-level storm flow is nearly axisymmetric and angular momentum does not change significantly with altitude, above the boundary layer conservation of angular momentum (neglecting vertical advection) gives us

$$u = -\frac{\partial M/\partial t}{\partial M/\partial r}. \tag{9}$$

Integrating the mass continuity equation [(3)] up from the top of the boundary layer gives

$$w_H = w_b + w_t, \tag{10}$$

where

$$w_t = \int_b^H \frac{1}{r}\frac{\partial}{\partial r}\left(r\frac{\partial M/\partial t}{\partial M/\partial r}\right)dz \simeq H_b\frac{1}{r}\frac{\partial}{\partial r}\left(r\frac{\partial M/\partial t}{\partial M/\partial r}\right), \tag{11}$$

where H_b ($H_b = H - b$) is a representative depth scale of the lower troposphere, and the subscript t is meant to denote the component of w arising from time dependence of the vortex.

Finally, we estimate the contribution to the free-tropospheric vertical velocity from the interaction between the vortex and its sheared environment, that is, the baroclinic component. This baroclinic/shear component, denoted as w_s, is estimated as

$$w_s \simeq \frac{g}{c_p(T_s - T_t)(1-\epsilon_p)N^2}V\left(f + \frac{V}{r} + \frac{\partial V}{\partial r}\right)(\Delta\mathbf{V}_e \cdot \mathbf{j}), \tag{12}$$

where ϵ_p is the precipitation efficiency, c_p is the heat capacity of dry air, g is the acceleration of gravity, N is the buoyancy frequency for dry air, T_s is the surface temperature, T_t is the tropopause temperature, $\mathbf{j}$ is the unit vector pointing radially outward from the storm center, and $\Delta\mathbf{V}_e$ is the vector wind shear across the troposphere. Note that the baroclinic component calculated in (12) vanishes if either the wind shear or the storm's wind vanishes, and that this component of upward motion will be positive downshear from the storm center and negative upshear. This component is estimated from isentropic ascent and descent owing to the interaction of the vortex with the saturation entropy surfaces (see appendix for derivation). This isentropic ascent and descent is the major process contributing to the net vertical velocity induced by the interaction of the vortex with the environmental shear (Raymond 1992; Zhu et al. 2013). With approximations (i.e., $\epsilon_p \sim 0.5$, $c_p \sim 1000\,\text{J kg}^{-1}\,\text{K}^{-1}$, $g \sim 10\,\text{m s}^{-2}$, $N^2 \sim 4\times10^{-4}$, $T_s - T_t \sim 100\,\text{K}$) and wind shear estimated from the difference of the geostrophic wind $\mathbf{V}_g$ at 200 and 850 mb ($\mathbf{V}_{g,200\text{mb}} - \mathbf{V}_{g,850\text{mb}}$), (12) may be reduced to $w_s \simeq 0.5fV(\mathbf{V}_{g,200\text{mb}} - \mathbf{V}_{g,850\text{mb}})\cdot\mathbf{j}$ (1 mb = 1 hPa).

While there is no particular justification for doing so, we simply add a radiative cooling component w_r (set to $-0.005\,\text{m s}^{-1}$) to the vertical motion derived above, and write

$$w = w_H + w_s + w_r = w_f + w_h + w_t + w_s + w_r \tag{13}$$

with the frictional component w_f given by (6), the topographic component w_h by (7), the stretching component w_t by (11), and the baroclinic component w_s by (12). The rain rate is calculated from the upward motion (when $w > 0$) using

$$P_{\text{rate}} = \epsilon_p \frac{\rho_{\text{air}}}{\rho_{\text{liquid}}} q_s (w_f + w_h + w_t + w_s + w_r). \quad (14)$$

If w is negative (downward motion), P_{rate} is set to zero.

The inputs to TCR are the gradient wind V, total wind $\mathbf{V}$, wind shear ($\mathbf{V}_{g,200\text{mb}} - \mathbf{V}_{g,850\text{mb}}$), topography, and the saturation specific humidity q_s along the storm track. In our analysis, the gradient wind V is computed either from the numerical wind profile simulated by WRF (sections 3 and 4) or from analytical wind profiles given storm characteristics (section 5). We approximate $\mathbf{V}$ as the sum of the gradient wind and storm translation, and we apply the saturation specific humidity at the storm center at 900 mb to obtain an estimate of the vapor flux through that level. Both saturation specific humidity and wind shear are obtained from WRF in our analysis. We apply a digital elevation map at 0.25° × 0.25° resolution for the calculation of the topographic effect. Other model parameters include the precipitation efficiency ϵ_p, the height parameter H_b, the topographic wind threshold V_{th}, and the drag coefficient C_d. For simplification, we assume a fixed fraction ($\epsilon_p = 0.9$) of the vapor flux falls to the surface as rainfall, and we treat H_b, V_{th}, and C_d as calibration parameters. Specifically, we let H_b be 1 km (although theoretically it may be closer to 3 km), V_{th} be 30 m s^{-1}, and C_d be different constants for ocean and land that are adjusted based on observations. The model is highly sensitive to C_d and the estimation over mountainous regions is sensitive to V_{th}, as discussed in section 5.

3. Model evaluation

Zhu et al. (2013) evaluated TCR's ability to capture TC rainfall statistics with gauge-based observations. Here we evaluate TCR with simulations of Hurricanes Isabel (2003) and Irene (2011) from the high-resolution numerical WRF Model to examine TCR's ability to capture major TC rainfall characteristics on an event basis.

The WRF Model is a mesoscale weather prediction system designed for both atmospheric research and operational forecasting. It has been widely used to study TC characteristics (e.g., Davis et al. 2008; Lin et al. 2010b; Huang et al. 2014; Liu and Smith 2016). In this study, the Advanced Research version of WRF (ARW), version 3.4.1, is used to simulate Hurricanes Isabel (2003) and Irene (2011), with the single-moment 6-class microphysics scheme, Yonsei University planetary boundary layer scheme, Monin–Obukhov surface-layer scheme, Noah land surface scheme, Dudhia shortwave scheme, and Rapid Radiative Transfer Model longwave scheme. For the purpose of evaluating TCR, our WRF simulations start about 18 h before landfall, covering regions of impact over both the ocean and land. Three nested simulation domains are used. Hourly outputs from the second domain (with horizontal grid size of 4 km) are used to prepare inputs for TCR, including information on track (track center determined with sea level pressure at each time step), wind at 900 mb (approximately the gradient level), specific humidity at 900 mb (at storm center), and environmental wind shear (between 850 and 200 mb, averaged over the 200–500-km annulus around the storm center). Specifically, the gradient wind V is computed by azimuthally averaging the azimuthal component of WRF wind at 900 mb after subtracting the background wind (approximated by 0.55 times the translational speed; Lin and Chavas 2012). This gradient wind is further smoothed with a 20-km moving average to reduce noise (discussed in section 5). Optimal drag coefficients are applied in TCR (C_d = 0.00125 over ocean and $C_d = 0.0016$ over land for Isabel; $C_d = 0.001$ over ocean and $C_d = 0.002$ over land for Irene; sensitivity to C_d is discussed in section 5). The value of P_{rate} in TCR is computed hourly and compared with hourly rainfall from WRF in terms of radial distribution of azimuthally averaged rainfall (section 3a), spatial distribution of rainfall (section 3b), and flood peaks (when coupled with a hydrological model; section 3c).

a. *Radial distribution of azimuthally averaged rainfall*

The radial distribution of azimuthally averaged rainfall is a primary metric in TC rainfall characterization and is frequently used in TC rainfall studies with observations (e.g., Lonfat 2004), global climate models (e.g., Villarini et al. 2014a), and downscaling simulations (e.g., Wright et al. 2015). It is also used in Langousis and Veneziano (2009a) as the primary metric in evaluating their theoretical TC rainfall model using high-resolution numerical simulations. Furthermore, R-CLIPER was developed by analyzing radial distributions of azimuthally averaged rainfall from satellite observations (Lonfat 2004; Lonfat et al. 2007) and has been used as a benchmark for evaluating TC rainfall forecasts from full numerical simulations (Tuleya et al. 2007).

The radial distribution of azimuthally averaged rainfall estimated for Hurricanes Isabel and Irene by TCR and WRF are compared in Fig. 1. As in previous studies on radial distributions of azimuthally averaged rainfall (e.g., Langousis and Veneziano 2009a), a time-averaging window (18 h) is applied. The distance from the storm center r is rescaled by the radius of maximum wind R_m to account for the evolving size of the storm. In general, TCR successfully captures the WRF-generated radial distribution of azimuthally averaged rainfall, including

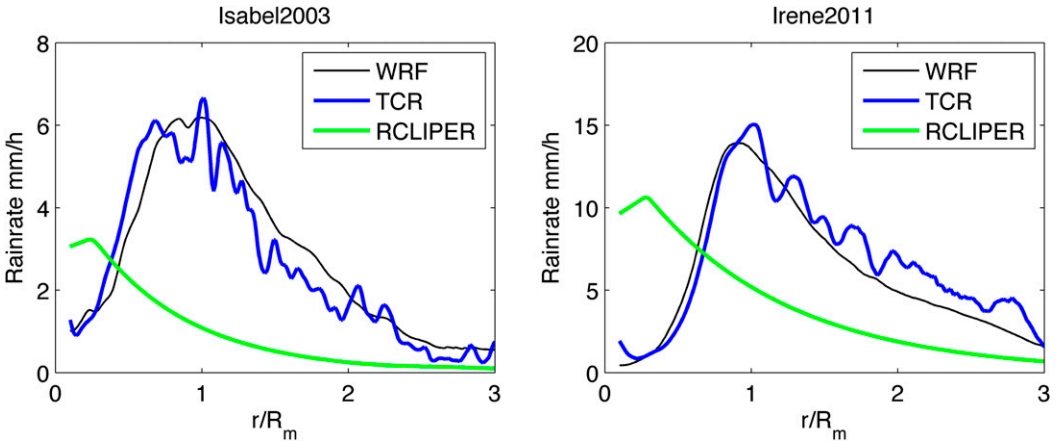

FIG. 1. Comparison of rainfall profile from WRF, TCR, and R-CLIPER for Hurricanes (left) Isabel and (right) Irene. The x axis shows the rescaled radius over the radius of maximum wind R_m. The rainfall profiles are averaged over 18 h during and after landfall (from 1200 UTC 18 Sep to 0500 UTC 19 Sep 2003 for Isabel and from 0600 to 2300 UTC 27 Aug 2011 for Irene). Parameters used in TCR are $H_b = 1$ km, $V_{th} = 30\,\mathrm{m\,s^{-1}}$, and $C_d = 0.001\,25$ over ocean and $C_d = 0.0016$ over land for Isabel and $C_d = 0.001$ over ocean and $C_d = 0.002$ over land for Irene.

the rainfall peak and its location. In both TCR and WRF simulations, azimuthally averaged rain rates increase from nearly zero ($<1\,\mathrm{mm\,h^{-1}}$) at the storm center to a maximum in the vicinity of the radius of the maximum wind and then decrease to small values at large radii (about 1–2 $\mathrm{mm\,h^{-1}}$ at $r = 3R_m$). The sharp peak of rainfall (rain rate of about 6 $\mathrm{mm\,h^{-1}}$ for Isabel and about 14 $\mathrm{mm\,h^{-1}}$ for Irene around $r = R_m$) indicates the occurrence of the strongest convection around the eyewall.

It is noted that TCR yields radial fluctuations of rainfall (Fig. 1), which come from the roughness of the gradient wind input from WRF. As discussed in detail in section 5, TCR is highly sensitive to the gradient wind input: high-frequency fluctuations in the gradient wind are amplified through the radial and time derivatives of the angular momentum [(6) and (11)]. According to Kepert and Nolan (2014) and Kepert (2017), the great sensitivity of rainfall estimation to small oscillations in angular momentum comes from neglecting nonlinear advection terms [(2)], which act as a spatial filter with a scale of ~20 km. In this study, we try to solve this sensitivity problem by applying a 20-km-window moving average to the WRF gradient wind input, although some numerical fluctuations still exist. With a larger averaging window, these fluctuations would smooth out, but the radial distribution of azimuthally averaged rainfall would shift toward larger radii (see section 5).

As a comparison, the radial rainfall profile estimated using R-CLIPER (the "final version"; Tuleya et al. 2007), with input from WRF (maximum wind from the gradient wind profile at 900 mb), is also displayed in Fig. 1. R-CLIPER produces a much lower rainfall profile for both Hurricanes Isabel and Irene than TCR and WRF and greatly underestimates the peak rain rate. Also, the location of the peak rainfall in R-CLIPER is much closer to the storm center, while it is around the radius of the maximum wind in both TCR and WRF. As also noted by previous studies, R-CLIPER may underestimate rainfall for extreme events (such as Isabel and Irene), because of its ensemble-averaging nature and coarse dependence on storm characteristics and that the model was developed based on TRMM, which may be biased toward low values for high rainfall intensities (Tuleya et al. 2007; Langousis and Veneziano 2009a; Mudd et al. 2015; Rasmussen et al. 2013).

b. Spatial distribution of rainfall

In addition to the symmetric component (i.e., azimuthally averaged rainfall), the asymmetric component of rainfall is also an important characteristic. We evaluate TCR's ability to capture rainfall asymmetries by examining the spatial distribution of its rainfall estimates.

The spatial distributions of storm-accumulated rainfall generated by TCR and WRF are compared in Fig. 2. For Hurricanes Isabel and Irene, rainfall asymmetries are associated with high rainfall intensities on different sides of the track (Figs. 2a,c). TCR does a good job capturing high rainfall intensities (warm colored, >140 mm for Isabel, >250 mm for Irene) at the correct locations. For the WRF simulation of Isabel (Fig. 2a), high rainfall intensities are centered between 34° and 38°N to the right of the track, which is well captured by TCR (Fig. 2b). High rainfall intensities in the WRF simulation of Irene

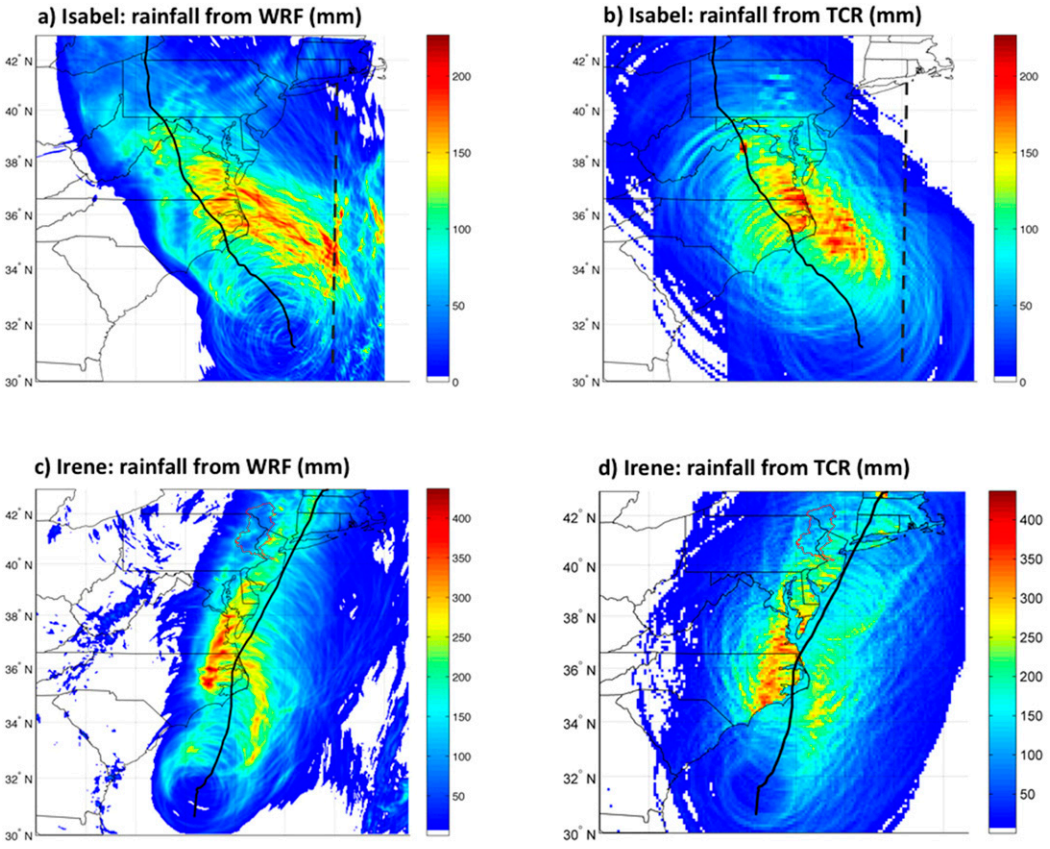

FIG. 2. Comparison of storm total rainfall accumulation (mm) estimated by (a),(c) WRF and (b),(d) TCR for Hurricanes (a),(b) Isabel and (c),(d) Irene. The dashed line in (a) and (b) indicates a reference location. The boundary of the Delaware River basin is outlined in red in (c) and (d). Parameters in TCR are as in Fig. 1.

(Fig. 2c), located along the coast between 35° and 40°N and over the ocean between 32° and 36°N, are also captured, although not precisely, by TCR (Fig. 2d). These rainfall asymmetries are induced by different rainfall mechanisms (discussed in section 4). Successful representations of these rainfall mechanisms are crucial for TCR to produce rainfall estimates with good spatial properties.

Not all the rainfall features in WRF simulations are captured in TCR. The moderate rainfall intensities to the east of Long Island (dashed line) in the WRF simulation of Hurricane Isabel (Fig. 2a) are missing in the TCR simulation (Fig. 2b). These rainfall intensities are located quite far from the track and are likely to be induced by other rain systems that are not represented in TCR. Also, rainfall from Isabel penetrates farther inland in WRF, which produces over 75 mm of rainfall in West Virginia (38°–41°N), to the left of the storm, while the rainfall is 35 mm less in TCR. It is likely that this asymmetry is associated with the extratropical transition of Isabel, which took place when Isabel moved over Pennsylvania (Lin et al. 2010b), while TCR does not account for all the effects of extratropical transition.

As for Hurricane Irene, the WRF simulation (Fig. 2c) shows a strong rainband between 32° and 34°N over the ocean. This rainband does not appear in the TCR simulation (Fig. 2d) since TCR does not resolve individual convective cells or spiral rainbands. Also, rainfall is more asymmetrically distributed north of 36°N (i.e., more concentrated on the left of the track) in WRF but more symmetric and extensive in TCR. It is possible that Irene started extratropical transition around 36°N (Grumm 2011; Liu and Smith 2016), which enhanced the asymmetry of rainfall. Another interesting observation is that TCR rainfall shows a sharp variation from water to land (especially around the Chesapeake Bay for Irene), while the spatial pattern in WRF is smoother. This unnaturally sharp variation of rainfall in TCR is caused by the different drag coefficients used over land and ocean and the lack of horizontal movement and mixing of the upward vapor flux (discussed in section 4).

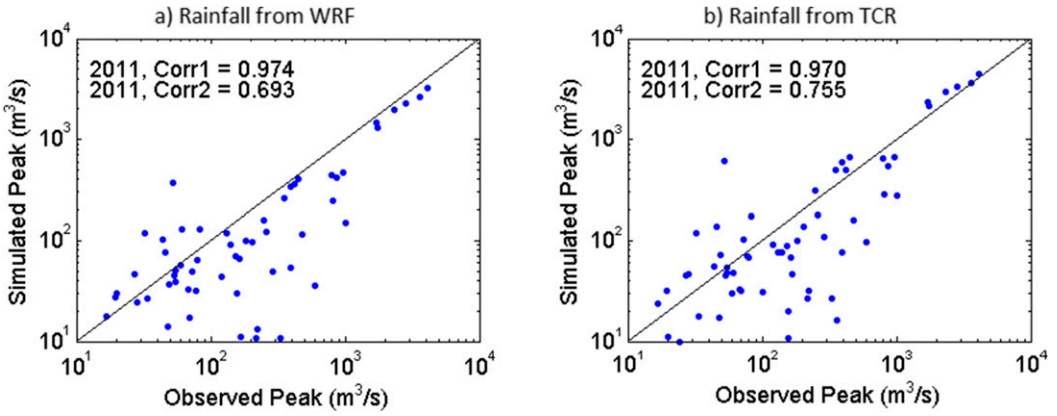

FIG. 3. Comparison of simulated vs observed flood peaks at 67 USGS stream gauging stations in the Delaware River basin for Hurricane Irene (2011), with rainfall forcing from (a) WRF and (b) TCR. Corr1 is the Pearson correlation between simulated and observed peaks; Corr2 is the Pearson correlation between the two in log scale. Parameters in TCR are as in Fig. 1.

c. *Flood peaks in the Delaware River basin*

Following our previous work on spatial characterization of floods in the Delaware River basin (Lu et al. 2017), we add one more process in the comparison of WRF and TCR: the hydrologic response. We apply the rainfall simulation for Hurricane Irene from WRF and TCR to a distributed, hillslope-based hydrologic model, CUENCAS (Mantilla and Gupta 2005; da Cunha 2012), and compare the simulated flood peaks over the Delaware River basin (basin boundary shown in Figs. 2c and 2d). Irene is one of the most significant flood events for the Delaware River basin, generating the fourth-largest flood peak at the basin outlet (Trenton) since the Great Flood of August 1955. Lu et al. (2017) showed that, with high-resolution radar rainfall fields as the principal forcing, CUENCAS captured the flood magnitudes over the Delaware River basin quite well for Irene and other flood events.

The simulated flood peaks in the Delaware River basin for Hurricane Irene with rainfall forcing from WRF and TCR are compared with observations from 67 USGS stream gauging stations (Fig. 3). As indicated by the scatterplots and correlation values (>0.97 in normal scale and >0.69 in log scale) shown in Fig. 3, simulated flood peaks from TCR rainfall are about as accurate as those from WRF rainfall. Simulated peak discharges with WRF rainfall shows systematic low bias (Fig. 3a) due to WRF's underestimation of rainfall in the central and lower portion of the basin (figure not shown). Curiously, the systematic low bias in peak discharges (as well as the underestimation of rainfall) is slightly improved in the TCR simulation (Fig. 3b). The large variations for small drainage areas (stations on small streams) in both cases are associated with uncertainties in rainfall estimates, antecedent soil moisture, and hydrologic model parameterization; these variations "average out" for greater drainage areas (stations on the mainstream), where simulated peaks compare very well with observations (with slight underestimation or overestimation with WRF or TCR rainfall forcing). It is noted that spatial distributions of rainfall in TCR exhibit deviations from those in WRF for Irene in the Delaware River basin (Figs. 2c,d). The similarity in the hydrologic simulation results indicates that the hydrologic processes, especially the flood peaks, are less sensitive to the spatial variation of rainfall.

4. Rainfall mechanisms

TC rainfall depends on various storm and environmental parameters in a complex way. It is difficult to decompose this complex dependence of TC rainfall in high-resolution numerical simulations or in observational products. For example, Fourier decomposition is widely used to study the effects of shear and storm motion on TC rainfall asymmetries (Lonfat et al. 2004; Chen et al. 2006; Ueno 2007; Wingo and Cecil 2010). However, the Fourier decomposition based on the observed or modeled rainfall fields cannot fully separate the various physical factors (storm motion, topography, wind shear, baroclinity, etc.) that jointly contribute to the rainfall asymmetry.

Given that TCR-estimated rainfall compares relatively well with WRF for both Hurricanes Isabel and Irene, in this section we examine the model components of TCR and investigate the modeled rainfall mechanisms for these two storms. As TCR estimates the rain rate directly from the upward vapor flux, we first

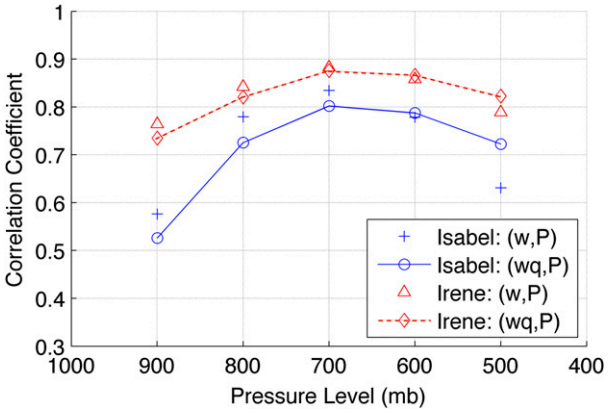

FIG. 4. Pearson correlation between azimuthally averaged precipitation P and upward vapor flux wq and between P and vertical velocity w at different pressure elevations in WRF simulations of Hurricanes Isabel and Irene, averaged over 18 h during and after landfall (from 1200 UTC 18 Sep to 0500 UTC 19 Sep 2003 for Isabel and from 0600 to 2300 UTC 27 Aug 2011 for Irene).

check the correlation between the two using the WRF simulations. Then, we examine the rainfall contributions from the four main vertical velocity components in TCR [(14)] that are related to frictional convergence w_f, vortex stretching w_t, topography w_h, and interaction with large-scale baroclinity or wind shear w_s.

a. P_{rate}–wq_s relationship

In TCR, rainfall P_{rate} is estimated by the upward vapor flux wq_s at a reference height [(1)]. Such a P_{rate}–wq_s relationship has been widely used to estimate heavy precipitation events [e.g., TC rainfall in Langousis and Veneziano (2009a), orographic precipitation in Alpert (1986), and monsoon-induced rainfall in Magagi and Barros (2004)]. This relationship represents the dominant mechanism of heavy precipitation—vertical moisture advection—while neglecting the relatively small contribution from local evaporation or change in the total column atmospheric water content due to horizontal advection (Wilson and Toumi 2005). The relationship also neglects the horizontal movement of raindrops. Here we evaluate this relationship by examining the correlation between rain rate and upward vapor flux in the WRF simulations for Irene and Isabel. Because the w field of WRF involves updrafts as well as downdrafts, to maintain physical realism for both, we use specific humidity q instead of saturated specific humidity q_s to compute vapor flux in this section. Numerically, q and q_s are very close (figure not shown).

First, we calculate the correlation coefficient of azimuthally averaged P_{rate} and wq within 600 km from storm center at different pressure levels (Fig. 4). Relatively high correlation is found for both Hurricanes Isabel and Irene. The maximum correlation (0.80 for Isabel and 0.88 for Irene) is obtained at 700 mb for both cases, consistent with Langousis and Veneziano's (2009a) MM5 simulation, in which the correlation of P_{rate} and wq reaches the maximum of 0.85 at 3 km (about 700 mb) for Hurricane Frances (2004). The correlation between P_{rate} and w, also shown in Fig. 4, reaches a slightly higher maximum (also at 700 mb) than the correlation between P_{rate} and wq, indicating the dominant role of w in determining the distribution of wq.

Then, to further examine the spatial variation, we construct the rain rate from WRF-simulated wq at 700 mb using (1) for Hurricanes Isabel and Irene. Figure 5 compares the total rainfall fields from the construction and WRF simulations. The 700-mb w field in WRF involves large positive and negative values, representing intense local updrafts and downdrafts of air associated with strong advection (figure not shown). These updrafts and downdrafts do not affect the correlation between the azimuthally averaged P_{rate} and wq, but they strongly affect the spatial distribution of the rainfall predicted by wq. As shown in Fig. 5, the accumulated rainfall field constructed from wq compares well with the accumulated rainfall field in WRF (Figs. 5a,d) only when a certain degree of smoothing is applied (Figs. 5b,e; wq smoothed with 22.5-km moving average). Without sufficient smoothing, the rainfall constructed from wq is very noisy and less informative (Figs. 5c,f; wq smoothed with 4.5-km moving average). This observation indicates that the $P_{\text{rate}}-wq$ (or $P_{\text{rate}}-wq_s$) relationship is not valid on very small horizontal scales, but it is a good approximation on scales where local evaporation and horizontal movement of raindrops are smoothed out. This observation also highlights the horizontal mixing of intense updrafts and downdrafts associated with individual convective cells that are represented in WRF but not in TCR.

TCR does not resolve individual convective cells, and thus the w field in TCR does not involve local intense updrafts/downdrafts, which favors the application of the $P_{\text{rate}}-wq_s$ relationship (note that the rain rate is set to zero for downdrafts). Still, the need exists for redistributing rainfall in TCR to account for the horizontal movement of raindrops during the time period when raindrops develop and fall. This time period is approximately 10–100 min (Langousis and Veneziano 2009a), which may be long enough for nonnegligible changes in spatial rainfall distributions to develop given strong horizontal winds in TCs. The horizontal redistribution of rainfall is considered in the MSR through correcting the modeled rainfall field (Langousis and Veneziano 2009a). A potential improvement of TCR is to include a similar correction to redistribute the modeled rainfall

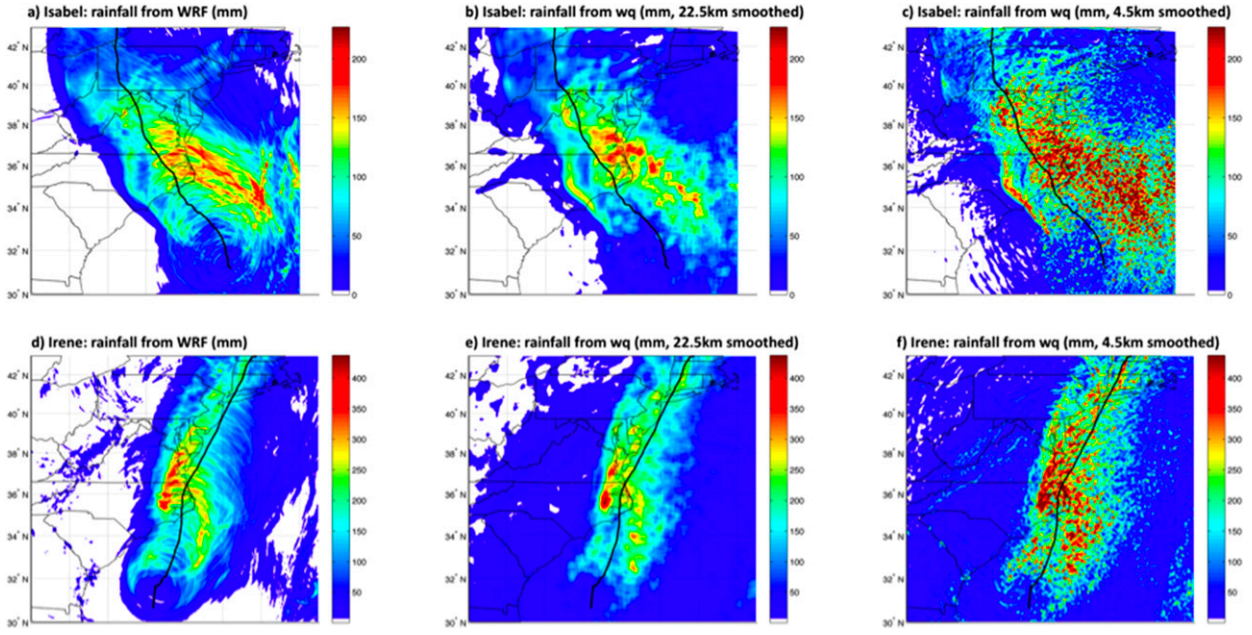

FIG. 5. Comparison of storm total rainfall distribution (mm) from (a),(d) WRF simulation to rainfall field constructed from upward vertical vapor flux wq from WRF at 700 mb using different moving-average parameters [(b),(e) 22.5 and (c),(f) 4.5 km] for Hurricanes (a)–(c) Isabel and (d)–(f) Irene. The rainfall field in (b), (c), (e), and (f) is constructed with (1).

field. We expect the redistribution process to also blur the sharp changes of rainfall at the coastline induced by different friction settings over land and ocean (e.g., around the Chesapeake Bay for Irene; Fig. 2d).

b. *Rainfall decomposition*

Among the various mechanisms considered in TCR [(14)], the frictional-convergence term dominates the total rainfall, contributing over 70% of storm rainfall for both Isabel (Fig. 6) and Irene (Fig. 7). The frictional effect depends on the gradient wind (including the background wind approximated by the storm translation) and a suitably defined drag coefficient [(6) and (8)]. Either stronger wind or a greater drag coefficient will yield a stronger upward motion at the top of the boundary layer, that is, more rainfall. Given a uniform surface roughness (drag coefficient), higher total wind to the right side of the track (in the Northern Hemisphere) results in more rainfall distributed to the right side of the track, as in the case of Isabel over both ocean and land (Fig. 6a). However, the spatial heterogeneity of the surface roughness can play an important role in shifting the distribution of friction-induced rainfall. Irene moved northeastward along the coast with land on its left and ocean on its right, and thus increased friction over land resulted in more rainfall distributed to the left of the track (Fig. 7a).

The vortex-stretching effect varies greatly with storm evolution. The vortex-stretching-induced term in TCR is a complex function of the radial and time derivatives of the angular momentum/azimuthal wind [(11)]. Generally speaking, storm intensification, which is associated with an inward shift of angular momentum surfaces (increasing maximum wind intensity and decreasing radius of maximum wind), leads to positive w_t (air lifting, more rainfall) at small radii and negative w_t (air descending, less rainfall) at large radii, and vice versa. The spatial distribution of rainfall from w_t features rings of rainfall at large radii for both Isabel (Fig. 6b) and Irene (Fig. 7b), indicating the weakening of the storm. Although these rings seem to come from irregularities of the input numerical wind profile, similar features appear when using smooth analytical wind profiles as input as well (figure not shown). The stretching term is very sensitive to different wind profiles, but the ring features always appear. The stretching term contributes approximately 30 mm to outer region rainfall for Isabel (Fig. 6b) and around 50 mm for Irene (Fig. 7b), each of which is about 1/5 of the magnitude of storm total rainfall (Figs. 2b,d).

The topographic effect is naturally most pronounced in mountainous regions. This effect in TCR depends on the magnitude of the horizontal wind and terrain gradient and the incidence angle of the flow on the terrain [(7)]. Isabel moved inland almost perpendicular to the Appalachians with cyclonic flow sweeping uphill to the right of the track, resulting in large topography-induced

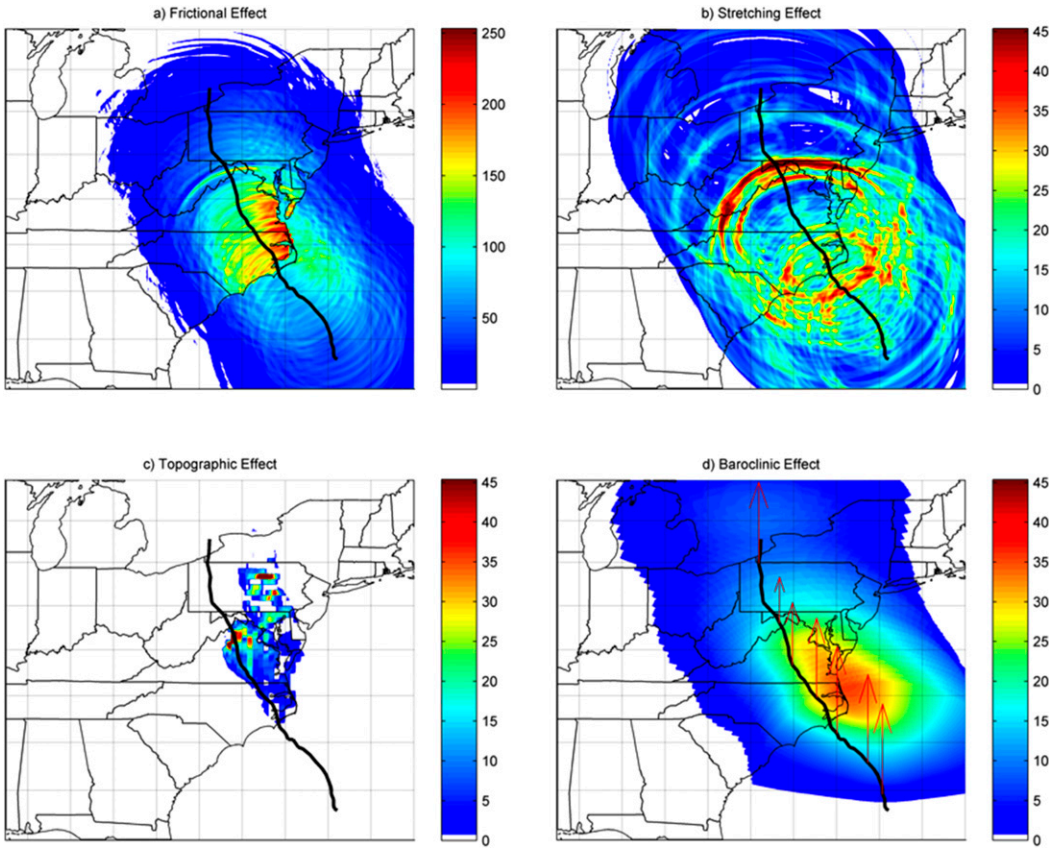

FIG. 6. Contribution to storm total rainfall accumulation (mm) from different mechanisms for Hurricane Isabel: (a) frictional effect, (b) stretching effect, (c) topographic effect, and (d) baroclinic effect. Directions of the environmental wind shear (computed with WRF outputs at 850 and 200 mb, averaged over the 200–500-km annulus from the storm center) are shown as arrows in (d). Note that the color bar in (a) is different from that in (b)–(d). Parameters in TCR are as in Fig. 1.

rainfall to the right of the track with a maximum of about 40 mm in northern Virginia and central Pennsylvania (Fig. 6c). In contrast, Irene moved almost parallel to the coast and the Appalachians, with cyclonic flow sweeping uphill to the left of the track, resulting in large topography-induced rainfall (about 30 mm) mostly to the left of the track (Fig. 7c). However, the maximum topography-induced rainfall (about 50 mm) occurred to the right of track when the storm later moved over land in western Connecticut, where the cyclonic flow interacted with the terrain (Fig. 7c). These results show that TCR can capture the main features of the topographic effect. Here, the rainfall estimation is limited by the relatively low resolution of the topography (0.25° × 0.25°), which, however, may partially compensate for the neglected smoothing due to advection of rain cells. Also, we may have underestimated rainfall in mountainous regions because 1) we applied a constant drag coefficient on land, while the surface of mountainous regions is usually rougher than that of flat land surfaces (Garratt 1977), leading to stronger friction-induced upward motion over the mountainous regions, and 2) we applied a constant precipitation efficiency (0.9), while orographic lifting is associated with increased precipitation efficiency (Huang et al. 2014), resulting in more rain over the mountains.

The magnitude of rainfall from the baroclinic or shear term (~30 mm for Isabel and ~50 mm for Irene; Figs. 6d, 7d) is close to that from the stretching or topographic term in TCR. As shown in Figs. 6d and 7d, the shear-induced rainfall in TCR is distributed in the downshear direction. Also, the asymmetric pattern of rainfall accumulation relative to the storm motion is largely affected by the shear direction relative to the storm motion (Rogers et al. 2003). For Isabel, the shear vector points to the front right relative to storm motion, resulting in the shear-induced rainfall distributed to the right of the track (Fig. 6d); for Irene, the shear vector points to the right of the storm motion before the first landfall in North Carolina and becomes parallel to the

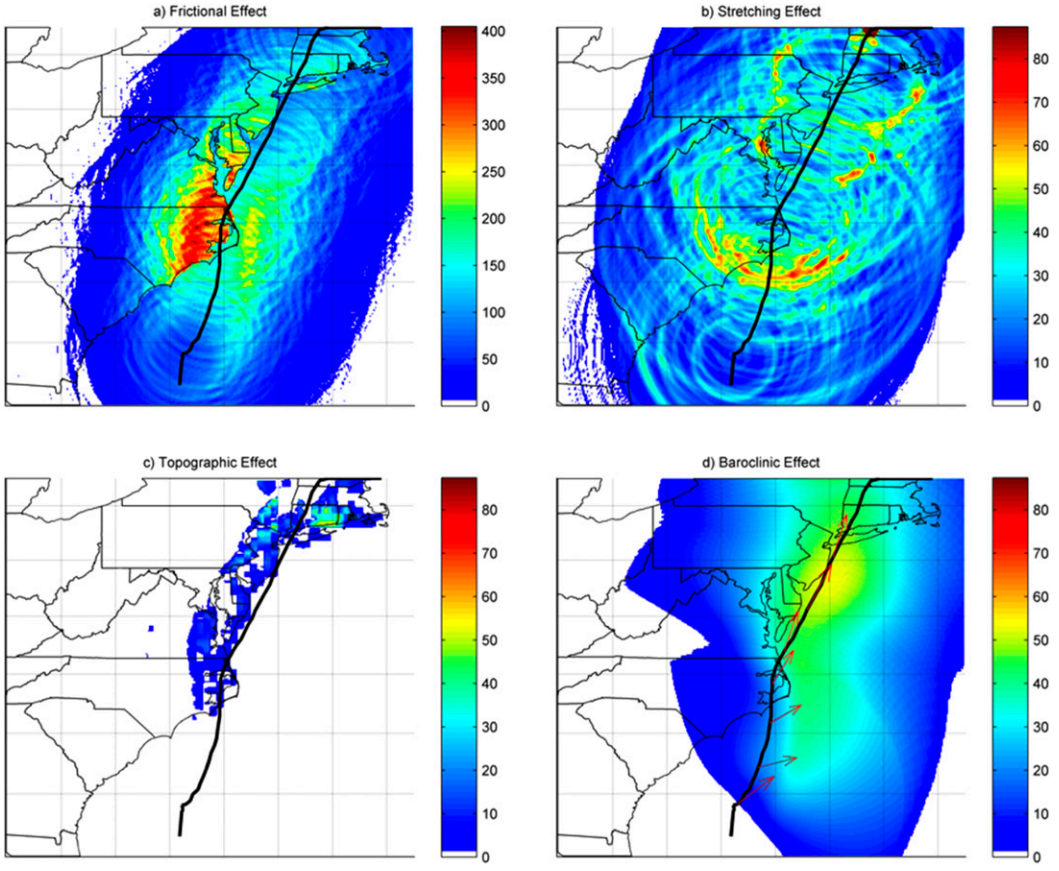

FIG. 7. As in Fig. 6, but for Hurricane Irene.

storm track afterward, leading to the shear-induced rainfall distributed asymmetrically to the right of the track before the first landfall and more symmetrically across the storm track afterward. These shear-induced asymmetrical features represented in TCR are generally consistent with real observations (Rogers et al. 2003; Chen et al. 2006; Wingo and Cecil 2010). Also, the baroclinic/shear term in TCR [which depends on the magnitude of the storm wind and the environmental wind shear as well as their relative angle; (12)], is mathematically similar to the first-order Fourier decomposition of rainfall in the shear-relative coordinate (Lonfat 2004; Lonfat et al. 2007), which confirms the consistency between the physics-based estimation in TCR and the statistics-based analyses in previous studies (e.g., Chen et al. 2006).

5. Sensitivity analysis

In this section, we investigate TCR's sensitivity to model inputs and parameters. As mentioned above, TCR is highly sensitive to the wind input. Here we further discuss the sensitivity of TCR to the smoothness of the numerical wind profile from the WRF simulation. We also examine the sensitivity of TCR to different analytical wind profiles, which is highly relevant to the application of TCR. Moreover, we discuss the sensitivity of TCR to two model parameters: the drag coefficient C_d and the topographic wind threshold V_{th}.

a. *Sensitivity to gradient wind*

1) SMOOTHING OF NUMERICAL WIND PROFILES FROM WRF

As shown in Fig. 1, with the numerical gradient wind profile generated by WRF as input, TCR yields notable fluctuations in the radial profile of rainfall. We examine the cause of these fluctuations by smoothing the numerical wind profile with different moving-average windows and compare the resulting TCR estimates of rainfall profiles (Figs. 8a,b). Without any smoothing, TCR estimates compare reasonably with WRF estimates within the eyewall ($r/R_m < 1$) but fluctuate greatly and stray from WRF estimates in outer regions

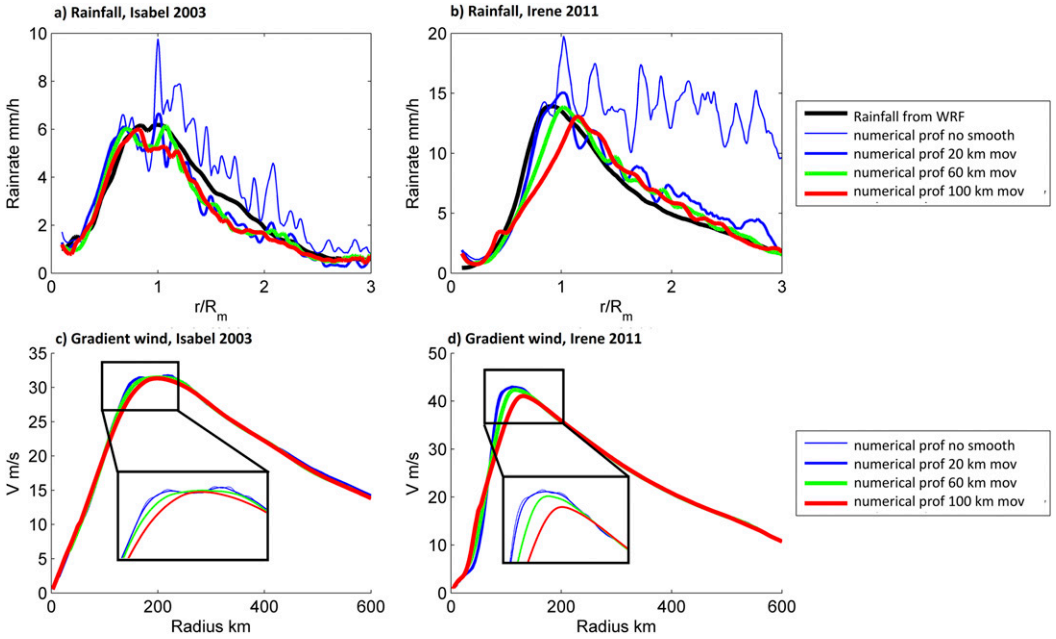

FIG. 8. (a),(b) Comparison of 18-h-averaged rainfall profile from WRF and from TCR with different empirical gradient wind inputs: wind profile from WRF at 900 mb with no smoothing and smoothed with an averaging window of 20 (as in Fig. 1), 60, and 100 km for Isabel and Irene. (c),(d) Comparison of the different empirical gradient wind profile inputs for Isabel (at 1400 UTC 18 Sep 2003) and Irene (at 1300 UTC 27 Aug 2011). The inset shows an enlarged view of the fluctuations of V around R_m. Except for the wind profile, parameters in TCR are as in Fig. 1.

($r/R_m \geq 1$), especially for Irene (Fig. 8b). A 20-km moving average of the gradient wind can greatly improve the results, producing reasonable rainfall estimates and greatly reduced variations. Radial variations of rainfall can be further reduced by further smoothing the gradient wind (e.g., with a 60- or 100-km window for the moving average), but the peak rainfall may be underestimated and shifted to larger radii because of the smoothing of the vortex (Figs. 8a,b). One may also use more sophisticated smoothing operations, for example, time averaging, to prepare the wind input for TCR from WRF.

TCR is highly sensitive to fluctuations in the gradient wind since it involves computing time and radial derivatives of the angular momentum [(6) and (11)], which can amplify any small irregularities in the wind input. This sensitivity can be highlighted by comparing the different WRF numerical wind inputs and the resulting TCR rainfall estimates (Fig. 8). Figures 8c and 8d show the WRF gradient wind profiles with different moving-average windows, which are used as input for TCR rainfall estimates in Figs. 8a and 8b, or Isabel and Irene, respectively. The different wind profiles appear quite similar, with notable differences only around the peak area, but they induce large differences in the entire rainfall profiles in TCR. (Although Figs. 8c and 8d show the gradient wind profiles at specific times, rather than averaged over the 18-h time window as for the rainfall profiles, similar features are observed for other time steps during the 18-h time period.) These contrasting results emphasize the need for a consistent preprocessing of the numerical wind input for TCR. In this study, a 20-km moving average, which is consistent with boundary layer theory (Kepert 2017) and the need to reduce noise without significantly modifying the vortex structure, is used as a default if not otherwise specified.

2) ANALYTICAL WIND PROFILES

Analytical wind profiles, also called parametric wind profiles, provide radial distributions of hurricane wind based on storm characteristics such as symmetrical maximum wind speed V_m and radius of maximum wind R_m. The wind profile may be mainly or partially empirical (Jelesnianski 1966; Holland 1980, hereafter H80; Holland et al. 2010) or mainly theoretical (Emanuel 2004, hereafter E04; Emanuel and Rotunno 2011, hereafter ER11; C15). The H80 profile, the most widely used analytical wind profile, is based on the gradient wind balance assumption and an empirical exponential distribution of storm pressure. It is extended in Holland et al. (2010) with a capacity to incorporate additional wind observations. E04 derived wind models for the

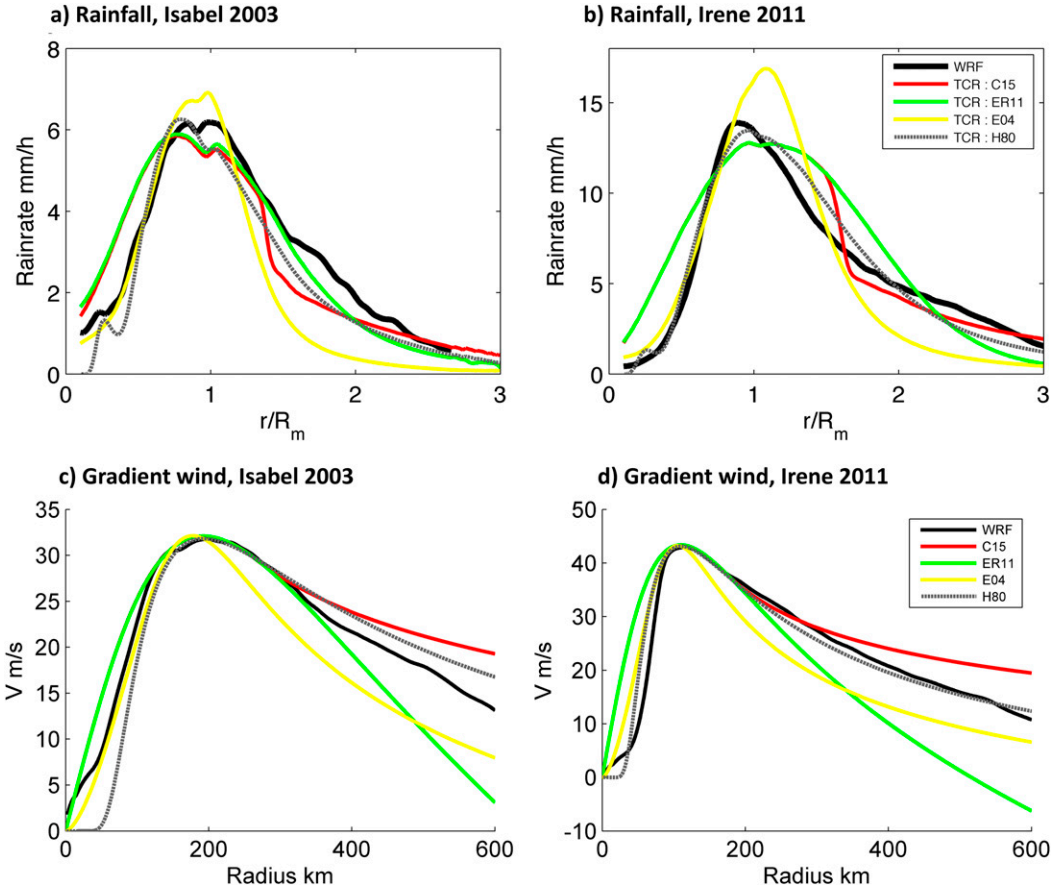

FIG. 9. (a),(b) Comparison of 18-h-averaged rainfall profile from WRF and from TCR with different analytical gradient wind inputs: theoretical wind profile from C15, ER11, E04, and H80. (c),(d) Comparison of different analytical gradient wind profile inputs for Isabel (at 1400 UTC 18 Sep 2003) and Irene (at 1300 UTC 27 Aug 2011). Except for the wind profile, parameters in TCR are as in Fig. 1.

outer nonconvecting region based on the free-tropospheric thermodynamic balance and boundary layer Ekman dynamic balance and for the inner convecting region based on boundary layer angular momentum balance and entropy quasi-equilibrium. ER11 derived an improved solution for the inner convecting region (still outside the eyewall) that arises from stratification of the outflow due to Kelvin–Helmholtz turbulence generated by the storm. C15 evaluated E04 and ER11 with historical observations and found that the outer nonconvecting region of E04 and the inner convecting region of ER11 are capable of reproducing the observed wind structure, and thus they mathematically merged the inner region of ER11 and the outer region of E04 to create a complete radial wind profile.

Analytical wind profiles are simple and computationally efficient; therefore, they are frequently used in risk assessment (Vickery et al. 2009; Lin et al. 2010a, 2012; Lin and Chavas 2012). The practical merit of analytical wind profiles goes along with our simple, computationally efficient TCR. For future risk assessment of rainfall and inland flooding, TCR will be coupled with analytical wind profiles for large numbers of simulations. Given that TCR is highly sensitive to the wind input, it is important to understand how TCR responds to different analytical wind profiles. We apply four widely used analytical wind profiles that are discussed above, namely, H80, E04, ER11, and C15, with storm characteristics (V_m and R_m) estimated from the numerical wind profile from WRF at the gradient level (900 mb), for Hurricanes Isabel and Irene.

TCR generally captures the azimuthal mean and spatial distribution of rainfall with different analytical wind profiles (Figs. 9a,b, 10). The rainfall estimates are closely related to the characteristics of the wind profiles (Figs. 9c,d) and have roots in the physical regimes of the wind models, since rainfall is closely tied to wind in the hurricane thermodynamics. Among the analytical wind

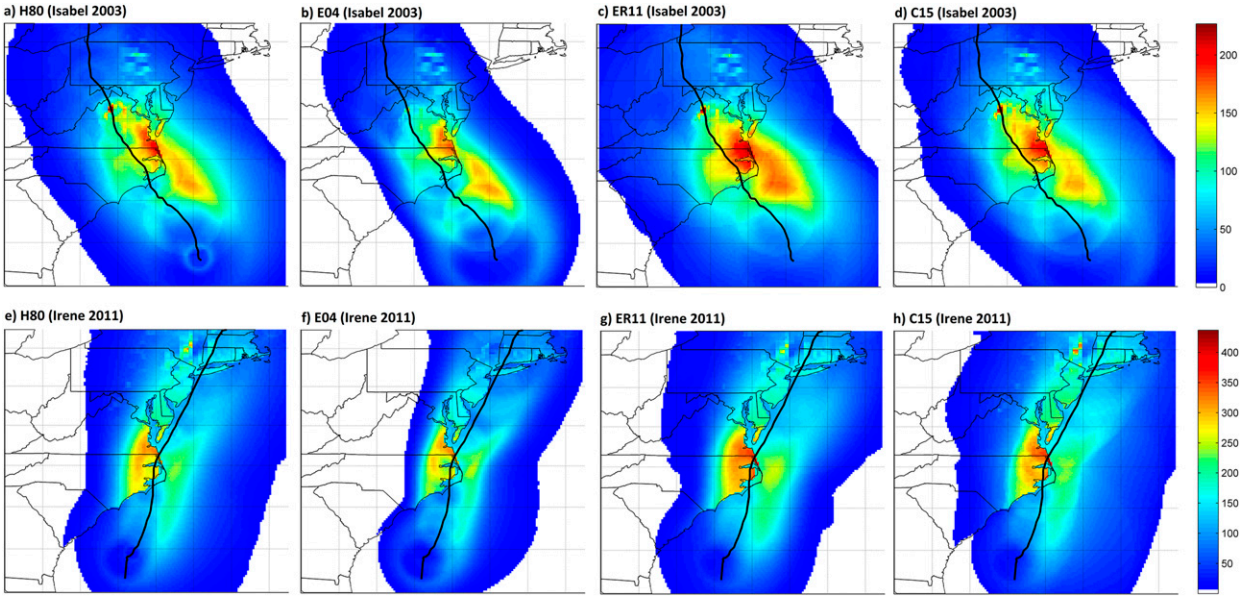

FIG. 10. Comparison of storm total rainfall accumulation (mm) estimated by TCR for Hurricanes (a)–(d) Isabel and (e)–(h) Irene with different analytical wind profiles from H80, E04, ER11, and C15.

profiles, H80 gives the best azimuthally averaged rainfall estimates compared to WRF for both the inner and outer regions for both Hurricanes Isabel and Irene (Figs. 9a,b). This is not very surprising since H80's radial wind profile is the closest to WRF's wind profile (Figs. 9c,d). The spatial distributions of storm total accumulated rainfall generated by TCR with H80 (Figs. 10a,e) also compares well with WRF (Fig. 2), capturing rainfall asymmetries at the correct locations. H80's ability to produce the right rainfall in TCR in turn indicates to some extent that H80's bases—gradient wind balance assumption and the exponential pressure distribution—are physically sound.

Rainfall estimates using E04 exhibit the largest deviations from WRF for both storms (Figs. 9a,b), with significant overestimation around $r = R_m$ and underestimation for $r > 1.5R_m$. The underestimation is likely due to E04's significant underestimation of the gradient wind at radii beyond R_m (Figs. 9c,d). The overestimation in the rainfall peak is likely due to the overestimation of the radial gradient of the wind ($\partial V/\partial r$) around R_m in E04. In terms of spatial distribution (Figs. 10b,f), accumulated rainfall from E04 is smaller compared to WRF and other wind profiles. The opposing effect of overestimation around R_m and underestimation for $r > 1.5R_m$ results in overall underestimation in storm accumulated rainfall, likely because the underestimation at large radius is associated with larger areas. Indeed, while the outer nonconvecting region of E04 has been shown to be useful for predicting storm structure in both idealized modeling (Chavas and Emanuel 2014) and observations (C15), the inner convecting region (where most precipitation takes place, including many of the radii shown in Figs. 9c and 9d) is not an advantage of E04 and has been improved in ER11.

Compared to E04, ER11 is associated with a lower magnitude of $\partial V/\partial r$ around R_m and higher magnitude of $\partial V/\partial r$ outward of R_m (associated with substantial underestimation of wind; Figs. 9c,d), leading to a smaller peak rainfall at $r = R_m$ and more rainfall distributed outward of R_m ($1.2R_m < r < 3R_m$) for both storms (Figs. 9a,b). In terms of spatial distribution, the opposing effect of underestimation around R_m and overestimation for $r > 1.2R_m$ results in overall overestimation in storm accumulated rainfall, likely due to the fact that the overestimation of the large radius is associated with larger areas (Figs. 10c,g).

The overestimation of rainfall beyond R_m (as well as substantial underestimation of wind) with ER11 is significantly improved in C15. By mathematically merging ER11 with E04, C15 gives a lower magnitude of the radial gradient of the wind (although higher winds) outside of the merge point (around $1.5R_m$) than ER11 (Figs. 9c,d), resulting in a smaller rainfall estimate than ER11 ($1.5R_m < r < 2R_m$; Figs. 9a,b). This improvement is also significant in spatial distribution of storm total accumulated rainfall (Figs. 10d,h). This decrease in rainfall from ER11 to C15 has roots in the physical regimes: beyond the merge point, C15 transitions from the inner convecting region of ER11 (corresponding to convective precipitation) to the outer nonconvecting

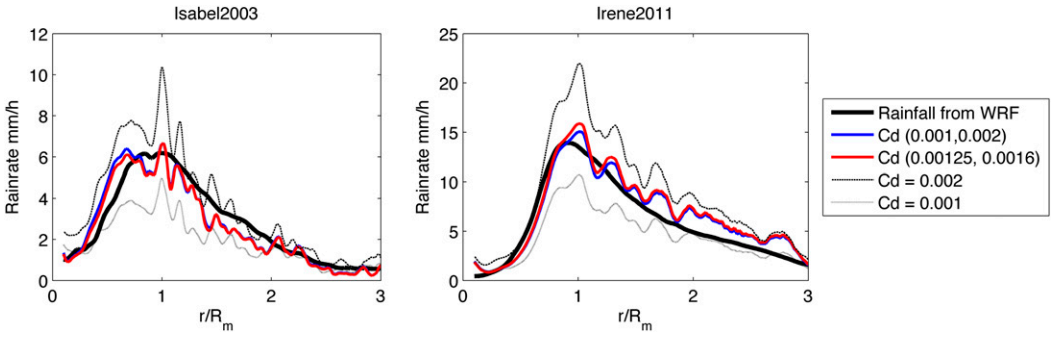

FIG. 11. Comparison of 18-h-averaged rainfall profile from WRF and from TCR with different drag coefficient for (left) Isabel and (right) Irene: C_d = 0.001, C_d =0.002, C_d = 0.001 over ocean and 0.002 over land (as in Fig. 1 for Irene), and C_d = 0.001 25 over ocean and 0.0016 over land (as in Fig. 1 for Isabel). Except C_d, parameters in TCR are as in Fig. 1.

region of E04 (corresponding to stratiform precipitation or clear skies), which naturally leads to less rainfall than in ER11. The sharpness of the decrease of rainfall around $1.5R_m$ with C15 (Figs. 9a,b) is induced by the transition of the wind profile in the vicinity of the merge point and is a result of the fact that the nature of the profile changes significantly (but smoothly) in the vicinity of the merge point.

It is worth mentioning the contrasting responses of TC rainfall modeling and surge modeling to the wind input. While storm surge is largely determined by the magnitude of the wind around the eyewall region and storm surge generally increases with increasing wind speed (Lin and Chavas 2012), TC rainfall depends also on the radial gradient of the wind. This difference is especially clear when comparing surge and rainfall estimates with E04 and ER11 wind inputs. Given the same storm characteristics (i.e., R_m and V_m), E04 produces smaller winds V than ER11 around the eyewall [shown for Isabel and Irene in Figs. 9c and 9d and for other storms in Fig. 4 of Lin and Chavas (2012)], which results in lower surge estimates with ER04 than with ER11 [~11% and 13% lower for two study sites in Lin and Chavas (2012)]. However, E04 is associated with a greater radial gradient of the wind around the eyewall, which results in a higher peak than ER11 in rainfall estimates (~30% higher for Isabel and Irene; Figs. 9a,b).

b. *Sensitivity to surface drag coefficient C_d*

The drag coefficient C_d is a dimensionless parameter that is used to quantify surface friction and is thus directly related to frictional convergence, the most important mechanism in TC rainfall production. It is also an important parameter in modeling hurricane intensity (in the theory of potential intensity; Emanuel 1986), wind structure (in analytical wind profiles such as E04, ER11, and C15), and storm surges (Lin and Chavas 2012). Here we examine the sensitivity of rainfall modeling to C_d.

The drag coefficient is closely tied to surface properties, and it differs greatly over land and ocean. Land surfaces in general require a drag coefficient around 0.002, while typical low-relief topography and low mountains (peaks <0.5–1 km) require a drag coefficient around 0.003 (Garratt 1977). Over the ocean, the drag coefficient is often formulated as a function of wind speed and takes various forms in the literature (e.g., Garratt 1977; Large and Pond 1981; Powell et al. 2003; Bell et al. 2012). As summarized in Bryant and Akbar (2016), many (over 20) formulations already exist for C_d over the ocean, yet new studies are still emerging based on new observations.

In TC boundary layer modeling and rainfall modeling, C_d also varies in different studies. For example, Smith (2003) used C_d from Shapiro (1983; taking values greater than 0.0011) for his slab hurricane boundary layer modeling; Kepert (2010b) used C_d from Smith and Montgomery (2008; taking values between 0.0007 and 0.002) for his slab hurricane boundary layer modeling. Langousis and Veneziano (2009a) used $C_d = 0.002$ for their hurricane rainfall modeling [which is based on a modified hurricane boundary layer model of Smith (2003)] and noted the high sensitivity of estimated rainfall to the drag coefficient.

Although there is no agreement on the "best" C_d, the value of C_d varies within the range 0.001–0.002 in most existing formulations. Here we examine how TCR responds to C_d, taking values of 0.001 and 0.002, and find that doubling C_d generally results in doubling rainfall estimates for both Isabel and Irene (Fig. 11). Without clear guidance on the values of C_d, we calibrate C_d in TCR with WRF estimated rainfall. We do not compute C_d from WRF because WRF has a much more sophisticated boundary layer formulation than TCR. After

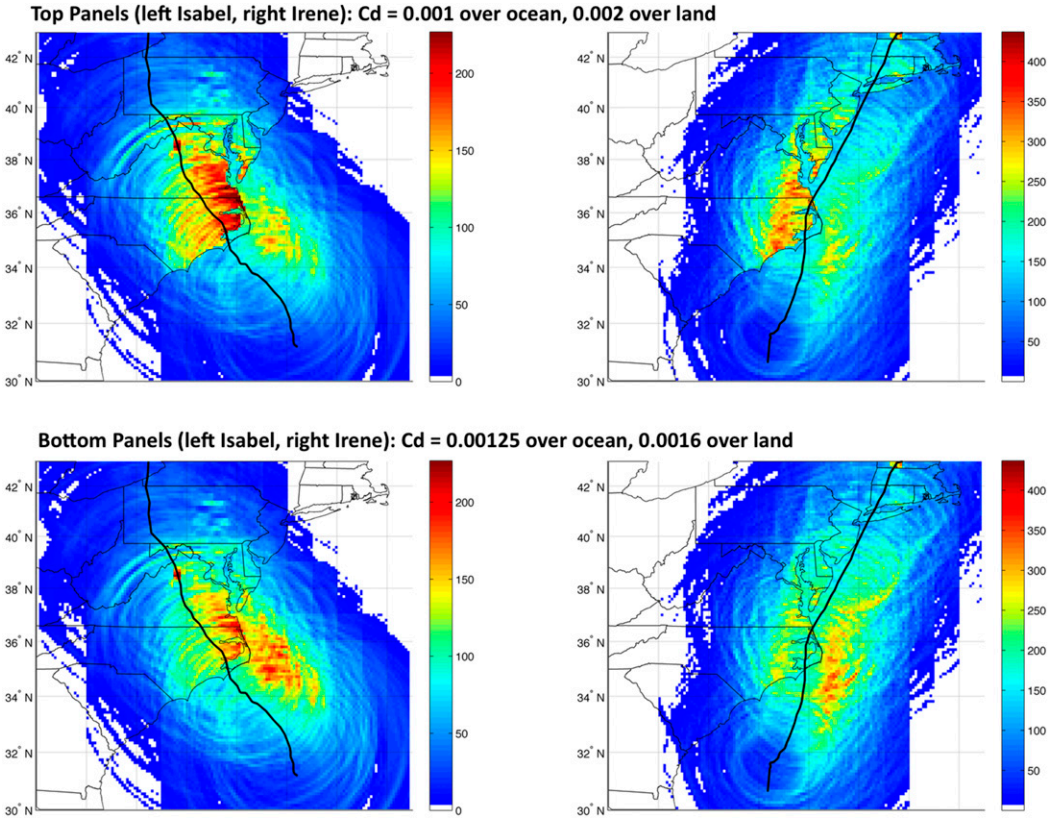

FIG. 12. Comparison of storm total rainfall accumulation (mm) from TCR for (left) Isabel and (right) Irene with different drag coefficients: (top) $C_d = 0.001$ over ocean and 0.002 over land; (bottom) $C_d = 0.001\,25$ over ocean and 0.0016 over land. Except C_d, parameters in TCR are as in Fig. 1.

trying a number of different C_d settings, we find that the optimal C_d setting differs for Isabel and Irene: $C_d = 0.001\,25$ over ocean and $C_d = 0.0016$ over land for Isabel, and $C_d = 0.001$ over ocean and $C_d = 0.002$ over land for Irene. These values of C_d may be relatively low, for example, compared to the value (0.002) used by Langousis and Veneziano (2009a) in their TC rainfall modeling, as the surface stress is calculated from the gradient wind, rather than the 10-m wind (with which C_d values are often associated), as noted earlier. Exchanging optimal C_d settings between the two cases results in small changes in the radial distribution of azimuthally averaged rainfall for both cases (Fig. 11, red and blue), but significant differences in the spatial distribution of rainfall (Fig. 12). The optimal C_d setting for Irene (Fig. 12, top; 0.001 over ocean, 0.002 over land) results in overestimated rainfall over land and underestimated rainfall over the ocean for Isabel. The optimal C_d for Isabel (Fig. 12, bottom; 0.001 25 over ocean, 0.0016 over land) results in the rainfall maximum shifting from the left to the right of the track for Irene. These changes indicate that the spatial distribution of rainfall is much more sensitive to the drag coefficient than is the azimuthal mean. Obtaining different optimal C_d settings for different storms also indicates to some extent that C_d has been used as a tuning parameter to compensate for errors induced by other uncertain parameters and/or neglected rainfall mechanisms (e.g., extratropical transition). Setting the "correct" drag coefficient in TCR demands further study.

c. *Sensitivity to the topographic wind threshold V_{th}*

One interesting finding in the model evaluation process is the necessity to reduce the topographic effect outside the storm core. For the study cases of Hurricanes Isabel and Irene, including a minimum cutoff threshold of about $30\,m\,s^{-1}$ for the horizontal wind in the topographic term in TCR produced reasonable results (Fig. 13). Without a sufficient wind threshold, TCR overestimates rainfall in the Appalachian regions (Fig. 13). Loosely speaking, the wind needs to be strong enough to climb up the hill, reach the condensation level, and generate topographic-induced rainfall. More theoretically, the elevation of an air parcel over topographic slopes

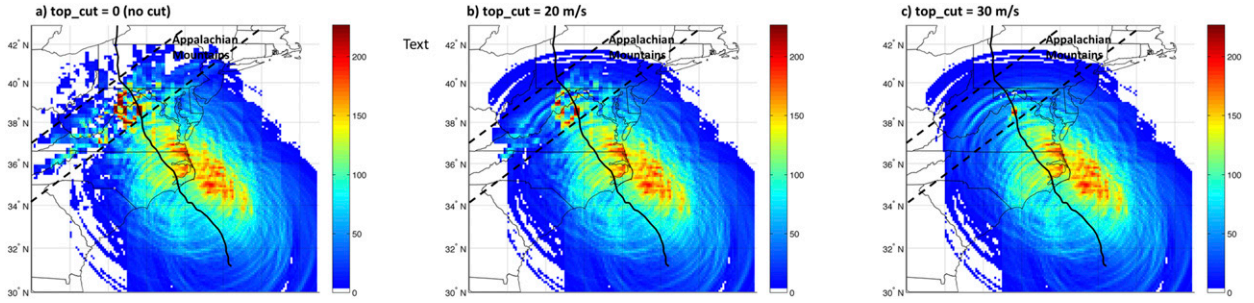

FIG. 13. Comparison of storm total rainfall accumulation (mm) from TCR for Isabel with different cutoff thresholds in computing the topographic effect: (a) 0, (b) 20, and (c) 30 m s^{-1}. Except the threshold, parameters in TCR are as in Fig. 1. The region of the Appalachian Mountains is denoted (dashed lines).

is associated with the gravity potential energy and the pressure potential energy of the flow, as depicted in the extended Froude number (Reinecke and Durran 2008). The effective Froude number is likely to be smaller in the storm core, where saturated air is ascending at near-neutral stability, than in the storm periphery. Here we avoid going into details about the Froude number and use a minimum wind threshold as a simple way to eliminate nonphysical rainfall outside the storm core over mountainous regions. The value of the selected threshold (30 m s^{-1}), however, may seem to be high, as it partially compensates for the simplified parameterization of saturated specific humidity, precipitation efficiency, surface roughness, and environmental background wind in the model.

6. Summary

We examine in detail a physics-based TC rainfall (TCR) model that generates spatial rainfall estimates along storm tracks, incorporating four major rainfall mechanisms: surface frictional convergence, vortex stretching, interaction of the storm with topography, and interaction of the storm with large-scale baroclinity (wind shear). TCR was initially developed as a fast algorithm for risk analysis (Emanuel et al. 2008; Emanuel 2017) and was shown to give long-term TC rainfall statistics comparable with gauge-based observations (Zhu et al. 2013). In this study, we evaluate TCR on an event basis with high-resolution numerical WRF simulations of Hurricanes Isabel (2003) and Irene (2011). With the WRF-generated storm characteristics and environment as input, TCR generates rainfall fields that compare well with WRF-estimated rainfall in terms of both azimuthal mean and spatial distributions. Also, when coupled with a hydrologic model (CUENCAS), TCR generates flood peaks over the Delaware River basin for Irene as accurately as WRF.

We then apply TCR to examine the various rainfall mechanisms for Hurricanes Isabel and Irene. Frictional convergence is shown to be the dominant mechanism, with the frictional-convergence term in TCR contributing over 70% of the total rainfall for both cases. However, the stretching, topographic, and baroclinic effects are also significant, with the related terms in TCR contributing around 10%–20% of the total rainfall. The vortex-stretching effect varies greatly with storm evolution, with storm intensification (weakening) often leading to positive (negative) contributions to the total rainfall at small radii and negative (positive) contributions at large radii. Thus, the stretching effect may have contributed to the rainfall at large radii for Isabel and Irene as they weakened during and after landfall. The topographic effect depends on the magnitude of the horizontal wind and terrain gradient and the incidence angle of the flow on the terrain, and it is shown to be different for Isabel and Irene given their different track orientation relative to the coast and the Appalachians. The baroclinic effect depends on the magnitude of the storm wind and the environmental wind shear as well as their relative angle, and it is shown to produce rain in the downshear direction. The shear-induced rainfall asymmetry as represented in TCR is generally consistent with previous observational studies.

As the surface frictional convergence term is the most important in TCR, the model is very sensitive to the drag coefficient C_d, which describes the surface roughness. This high sensitivity of TC rainfall to C_d is also noted in other TC rainfall models (e.g., Langousis and Veneziano 2009a). Optimal C_d values are used in our analyses. Although these values are reasonable based on previous studies, they are different for the two storms, indicating that to some extent C_d has been used as a tuning parameter to compensate for errors induced by other uncertain parameters and/or neglected rainfall mechanisms. Further study with more storm cases is needed to better set the drag coefficient in the model. In addition, it is found to be necessary for eliminating nonphysical rainfall over

mountainous regions outside the storm core. A minimum cutoff wind threshold of $30\,\mathrm{m\,s^{-1}}$ is simply applied to eliminate the nonphysical mountainous rainfall for the two storms. This method should also be further evaluated with more study cases.

A more important finding is that TCR is strongly sensitive to the wind input, as it involves computing the time and radial derivatives of the gradient wind. As a result, a smoothing (with a moving-average window of 20 km in the study cases) of the numerical wind profile from WRF before it is applied as an input to TCR is necessary for generating accurate rainfall estimates. TCR is also very sensitive to the details (e.g., smoothness) of analytical wind profiles. Several commonly used analytical wind profiles are tested and the Holland model (H80) is found to perform the best. While the Holland model is partially empirical, other more theoretical wind models also give good rainfall estimates, which may indicate to some extent that the theoretical assumptions under these wind models are correct, as the TC rainfall and wind are thermodynamically connected. The analysis with the various analytical wind profiles leads to another interesting finding: TC rainfall modeling responds to the wind input very differently from the surge modeling. While storm surge is largely determined by the magnitude of the winds around the eyewall region, such that stronger winds generally produce greater surge, TC rainfall relates to the winds in more complex ways (e.g., radial gradients, time evolution), such that it is possible that greater rainfall can be associated with weaker winds.

In addition to better estimating the model parameters, future model improvements may include redistributing rainfall due to horizontal movement of raindrops (Langousis and Veneziano 2009a), coupling TCR with boundary layer modeling for more accurate estimation of friction (Smith 2003; Smith and Montgomery 2010; Kepert 2010a,b, 2012; Langousis et al. 2008), and accounting for the spatial and temporal variations of precipitation efficiency and humidity. Similar to other TC rainfall models (e.g., R-CLIPER, PHRaM, and MSR), TCR does not account for rainfall fluctuations at small spatial scales (e.g., rainbands and local convective cells). Such small-scale variations may be added statistically, following Langousis et al. (2008) and Langousis and Veneziano (2009b). Given its high computational efficiency, TCR can be coupled with an analytical wind model (e.g., the Holland model), a hydrological model (e.g., CUENCAS), and a TC climatology model (e.g., Emanuel et al. 2008) to generate large numbers of synthetic events to assess the risk associated with TC rainfall and inland flooding under various climate conditions.

Acknowledgments. This material is based upon work supported by the National Science Foundation under Award 25204-G0001-10008127-AWD1004514. We thank three anonymous reviewers for helping to improve this work.

APPENDIX

Interaction of the Vortex with the Saturation Entropy Surfaces

We estimate the contribution to the free-tropospheric vertical velocity from the interaction between the vortex and its environment. Suppose that we place ourselves in a coordinate system moving with the storm center, and in the first place suppose that the storm circulation is steady in time. (We will relax this approximation later.) In the saturated regions of the storm, steadiness requires that the saturation moist entropy distribution remains stationary. This may be expressed as

$$\mathbf{V}\cdot\nabla s^{*}+w\frac{\partial s^{*}}{\partial z}=0, \tag{A1}$$

where s^{*} is the saturation moist entropy and $\mathbf{V}$ is the total vector horizontal wind relative to the moving storm. The second term in (A1) can be thought of as the rate of warming or cooling owing to vertical motion in a moist atmosphere. In a convecting system, Emanuel et al. (1994) argues that this term can be represented as a fixed fraction of the dry stratification:

$$\frac{\partial s^{*}}{\partial z}\simeq\left(1-\epsilon_{p}\right)\frac{\partial s_{d}}{\partial z}=\left(1-\epsilon_{p}\right)\frac{c_{p}}{g}N^{2}, \tag{A2}$$

where ϵ_p is the precipitation efficiency, s_d is the entropy of dry air, c_p is the heat capacity of dry air, g is the acceleration of gravity, and N is the buoyancy frequency for dry air. In (A1) we approximate both N and ϵ_p as constants and write

$$w\simeq-\frac{g}{c_{p}}\frac{\mathbf{V}\cdot\nabla s^{*}}{\left(1-\epsilon_{p}\right)N^{2}}. \tag{A3}$$

Now we divide up both the wind and saturation entropy fields into environmental and storm components, so that

$$\mathbf{V}\cdot\nabla s^{*}=\left(\mathbf{V}_{e}+\mathbf{V}_{\mathrm{TC}}\right)\cdot\nabla\left(s_{e}^{*}+s_{\mathrm{TC}}^{*}\right), \tag{A4}$$

where the subscripts refer to environmental and tropical cyclone (TC) quantities, and both vector winds are relative to the moving storm. We first note that $\mathbf{V}_{\mathrm{TC}}\cdot\nabla s_{\mathrm{TC}}^{*}=0$, since the storm's interior flow is orthogonal to the entropy gradient. We also neglect any vertical motion that would exist in the absence of the storm, taking $\mathbf{V}_{e}\cdot\nabla s_{e}^{*}=0$. Thus, we approximate (A4) as

$$\mathbf{V}\cdot\nabla s^{*}\simeq\mathbf{V}_{e}\cdot\nabla s^{*}_{\mathrm{TC}}+\mathbf{V}_{\mathrm{TC}}\cdot\nabla s^{*}_{e}. \tag{A5}$$

We further simplify (A5) as follows. First, we approximate the large-scale environmental flow as being in thermal wind balance. This may be written [see Emanuel 1995, their (23)]

$$\nabla s^{*}_{e}=\frac{f}{T_{S}-T_{t}}\mathbf{k}\times\Delta\mathbf{V}_{e}, \tag{A6}$$

where f is the Coriolis parameter, T_s is the surface temperature, T_t is the tropopause temperature, $\mathbf{k}$ is the unit vector in the vertical, and $\Delta\mathbf{V}_e$ is the vector wind shear across the troposphere. In deriving (A6), it has been assumed that the environmental temperature lapse rate is approximately moist adiabatic, which is bound to be the case in the environment of a tropical cyclone. At the same time, we assume that the interior tropical cyclone vortex is in gradient and hydrostatic balance, and that it is neutral to slantwise moist convection. Under these conditions, the horizontal gradient of saturation entropy in the vortex can be written [see Emanuel 1986, their (13)] as

$$\nabla s^{*}_{\mathrm{TC}}=\frac{-\mathbf{j}V}{T_{s}-T_{t}}\left(\frac{V}{r}+\frac{\partial V}{\partial r}\right), \tag{A7}$$

where $\mathbf{j}$ is the unit vector in the radial direction and V is the azimuthal gradient wind.

We next note that since the storm moves approximately with some vertically averaged environmental flow, the storm relative environmental wind should be proportional to the environmental wind shear $\Delta\mathbf{V}_e$, which is independent of the motion of the reference frame. Thus, we take $\mathbf{V}_e\simeq\Delta\mathbf{V}_e$. Finally, we note that since the storm wind is purely azimuthal, $\mathbf{V}_{\mathrm{TC}}=V(\mathbf{k}\times\mathbf{j})$. Using these relations and (A5)–(A7), we write (A3) as

$$w_{s}\simeq\frac{g}{c_{p}(T_{s}-T_{t})(1-\epsilon_{p})N^{2}}V\left(f+\frac{V}{r}+\frac{\partial V}{\partial r}\right)(\Delta\mathbf{V}_{e}\cdot\mathbf{j}). \tag{A8}$$

We affix the subscript s to the vertical velocity defined by (A8) to denote the component of w owing to the interaction of the storm with its sheared environment.

REFERENCES

Alpert, P., 1986: Mesoscale indexing of the distribution of orographic precipitation over high mountains. *J. Climate Appl. Meteor.*, **25**, 532–545, https://doi.org/10.1175/1520-0450(1986)025<0532:MIOTDO>2.0.CO;2.

Atallah, E., and L. F. Bosart, 2003: The extratropical transition and precipitation distribution of Hurricane Floyd (1999). *Mon. Wea. Rev.*, **131**, 1063–1081, https://doi.org/10.1175/1520-0493(2003)131<1063:TETAPD>2.0.CO;2.

Barstad, I., and R. B. Smith, 2005: Evaluation of an orographic precipitation model. *J. Hydrometeor.*, **6**, 85–99, https://doi.org/10.1175/JHM-404.1.

Bell, M. M., M. T. Montgomery, and K. A. Emanuel, 2012: Air–sea enthalpy and momentum exchange at major hurricane wind speeds observed during CBLAST. *J. Atmos. Sci.*, **69**, 3197–3222, https://doi.org/10.1175/JAS-D-11-0276.1.

Bryant, K., and M. Akbar, 2016: An exploration of wind stress calculation techniques in hurricane storm surge modeling. *J. Mar. Sci. Eng.*, **4**, 58, https://doi.org/10.3390/jmse4030058.

Chavas, D. R., and K. Emanuel, 2014: Equilibrium tropical cyclone size in an idealized state of axisymmetric radiative–convective equilibrium. *J. Atmos. Sci.*, **71**, 1663–1680, https://doi.org/10.1175/JAS-D-13-0155.1.

——, N. Lin, and K. Emanuel, 2015: A model for the complete radial structure of the tropical cyclone wind field. Part I: Comparison with observed structure. *J. Atmos. Sci.*, **72**, 3647–3662, https://doi.org/10.1175/JAS-D-15-0014.1.

Chen, S. S., J. A. Knaff, and F. D. Marks Jr., 2006: Effects of vertical wind shear and storm motion on tropical cyclone rainfall asymmetries deduced from TRMM. *Mon. Wea. Rev.*, **134**, 3190–3208, https://doi.org/10.1175/MWR3245.1.

Cheung, K. K. W., L.-R. Huang, and C.-S. Lee, 2008: Characteristics of rainfall during tropical cyclone periods in Taiwan. *Nat. Hazards Earth Syst. Sci.*, **8**, 1463–1474, https://doi.org/10.5194/nhess-8-1463-2008.

Czajkowski, J., K. Simmons, and D. Sutter, 2011: An analysis of coastal and inland fatalities in landfalling US hurricanes. *Nat. Hazards*, **59**, 1513–1531, https://doi.org/10.1007/s11069-011-9849-x.

——, G. Villarini, E. Michel-Kerjan, and J. A. Smith, 2013: Determining tropical cyclone inland flooding loss on a large scale through a new flood peak ratio-based methodology. *Environ. Res. Lett.*, **8**, 044056, https://doi.org/10.1088/1748-9326/8/4/044056.

——, ——, M. Montgomery, E. Michel-Kerjan, and R. Goska, 2017: Assessing current and future freshwater flood risk from North Atlantic tropical cyclones via insurance claims. *Sci. Rep.*, **7**, 41609, https://doi.org/10.1038/srep41609.

da Cunha, L. K., 2012: Exploring the benefits of satellite remote sensing for flood prediction across scales. Ph.D. thesis, University of Iowa, 245 pp. http://ir.uiowa.edu/etd/2848.

Davis, C., and Coauthors, 2008: Prediction of landfalling hurricanes with the Advanced Hurricane WRF Model. *Mon. Wea. Rev.*, **136**, 1990–2005, https://doi.org/10.1175/2007MWR2085.1.

Dietrich, J. C., and Coauthors, 2010: A high-resolution coupled riverine flow, tide, wind, wind wave, and storm surge model for southern Louisiana and Mississippi. Part II: Synoptic description and analysis of Hurricanes Katrina and Rita. *Mon. Wea. Rev.*, **138**, 378–404, https://doi.org/10.1175/2009MWR2907.1.

Elsberry, R. L., 2002: Predicting hurricane landfall precipitation: Optimistic and pessimistic views from the Symposium on Precipitation Extremes. *Bull. Amer. Meteor. Soc.*, **83**, 1333–1339, https://doi.org/10.1175/1520-0477(2002)083<1333:PHLPOA>2.3.CO;2.

Emanuel, K. A., 1986: An air–sea interaction theory for tropical cyclones. Part I: Steady-state maintenance. *J. Atmos. Sci.*, **43**, 585–605, https://doi.org/10.1175/1520-0469(1986)043<0585:AASITF>2.0.CO;2.

——, 1991: The theory of hurricanes. *Annu. Rev. Fluid Mech.*, **23**, 179–196, https://doi.org/10.1146/annurev.fl.23.010191.001143.

——, 1995: On thermally direct circulations in moist atmospheres. *J. Atmos. Sci.*, **52**, 1529–1534, https://doi.org/10.1175/1520-0469(1995)052<1529:OTDCIM>2.0.CO;2.

——, 2004: Tropical cyclone energetics and structure. *Atmospheric Turbulence and Mesoscale Meteorology*, E. Fedorovich, R. Rotunno, and B. Stevens, Eds., Cambridge University Press, 165–191, https://doi.org/10.1017/CBO9780511735035.010.

——, 2013: Downscaling CMIP5 climate models shows increased tropical cyclone activity over the 21st century. *Proc. Natl. Acad. Sci. USA*, **110**, 12 219–12 224, https://doi.org/10.1073/pnas.1301293110.

——, 2017: Assessing the present and future probability of Hurricane Harvey's rainfall. *Proc. Natl. Acad. Sci. USA*, **114**, 12 681–12 684, https://doi.org/10.1073/pnas.1716222114.

——, and R. Rotunno, 2011: Self-stratification of tropical cyclone outflow. Part I: Implications for storm structure. *J. Atmos. Sci.*, **68**, 2236–2249, https://doi.org/10.1175/JAS-D-10-05024.1.

——, J. D. Neelin, and C. S. Bretherton, 1994: On large-scale circulations in convecting atmospheres. *Quart. J. Roy. Meteor. Soc.*, **120**, 1111–1143, https://doi.org/10.1002/qj.49712051902.

——, R. Sundararajan, and J. Williams, 2008: Hurricanes and global warming: Results from downscaling IPCC AR4 simulations. *Bull. Amer. Meteor. Soc.*, **89**, 347–367, https://doi.org/10.1175/BAMS-89-3-347.

Garratt, J. R., 1977: Review of drag coefficients over oceans and continents. *Mon. Wea. Rev.*, **105**, 915–929, https://doi.org/10.1175/1520-0493(1977)105<0915:RODCOO>2.0.CO;2.

Grumm, R. H., 2011: Irene rains over the East Coast. Tech. Doc. 30 pp. http://cms.met.psu.edu/sref/severe/2011/28Aug2011.pdf .

Harr, P. A., and R. L. Elsberry, 2000: Extratropical transition of tropical cyclones over the western North Pacific. Part I: Evolution of structural characteristics during the transition process. *Mon. Wea. Rev.*, **128**, 2613–2633, https://doi.org/10.1175/1520-0493(2000)128<2613:ETOTCO>2.0.CO;2.

——, ——, and T. F. Hogan, 2000: Extratropical transition of tropical cyclones over the western North Pacific. Part II: The impact of midlatitude circulation characteristics. *Mon. Wea. Rev.*, **128**, 2634–2653, https://doi.org/10.1175/1520-0493(2000)128<2634:ETOTCO>2.0.CO;2.

Holland, G. J., 1980: An analytical model of the wind and pressure profiles in hurricanes. *Mon. Wea. Rev.*, **108**, 1212–1218, https://doi.org/10.1175/1520-0493(1980)108<1212:AAMOTW>2.0.CO;2.

——, J. I. Belanger, and A. Fritz, 2010: A revised model for radial profiles of hurricane winds. *Mon. Wea. Rev.*, **138**, 4393–4401, https://doi.org/10.1175/2010MWR3317.1.

Huang, H.-L., M.-J. Yang, and C.-H. Sui, 2014: Water budget and precipitation efficiency of Typhoon Morakot (2009). *J. Atmos. Sci.*, **71**, 112–129, https://doi.org/10.1175/JAS-D-13-053.1.

Jelesnianski, C. P., 1966: Numerical computations of storm surges without bottom stress. *Mon. Wea. Rev.*, **94**, 379–394, https://doi.org/10.1175/1520-0493(1966)094<0379:NCOSSW>2.3.CO;2.

Jones, S. C., and Coauthors, 2003: The extratropical transition of tropical cyclones: Forecast challenges, current understanding, and future directions. *Wea. Forecasting*, **18**, 1052–1092, https://doi.org/10.1175/1520-0434(2003)018<1052:TETOTC>2.0.CO;2.

Kepert, J. D., 2001: The dynamics of boundary layer jets within the tropical cyclone core. Part I: Linear theory. *J. Atmos. Sci.*, **58**, 2469–2484, https://doi.org/10.1175/1520-0469(2001)058<2469:TDOBLJ>2.0.CO;2.

——, 2010a: Slab- and height-resolving models of the tropical cyclone boundary layer. Part I: Comparing the simulations. *Quart. J. Roy. Meteor. Soc.*, **136**, 1686–1699, https://doi.org/10.1002/qj.667.

——, 2010b: Slab- and height-resolving models of the tropical cyclone boundary layer. Part II: Why the simulations differ. *Quart. J. Roy. Meteor. Soc.*, **136**, 1700–1711, https://doi.org/10.1002/qj.685.

——, 2012: Choosing a boundary layer parameterization for tropical cyclone modeling. *Mon. Wea. Rev.*, **140**, 1427–1445, https://doi.org/10.1175/MWR-D-11-00217.1.

——, 2013: How does the boundary layer contribute to eyewall replacement cycles in axisymmetric tropical cyclones? *J. Atmos. Sci.*, **70**, 2808–2830, https://doi.org/10.1175/JAS-D-13-046.1.

——, 2017: Time and space scales in the tropical cyclone boundary layer, and the location of the eyewall updraft. *J. Atmos. Sci.*, **74**, 3305–3323, https://doi.org/10.1175/JAS-D-17-0077.1.

——, and D. S. Nolan, 2014: Reply to ''Comments on 'How does the boundary layer contribute to eyewall replacement cycles in axisymmetric tropical cyclones?''' *J. Atmos. Sci.*, **71**, 4692–4704, https://doi.org/10.1175/JAS-D-14-0014.1.

Knutson, T. R., and R. E. Tuleya, 2004: Impact of CO_2-induced warming on simulated hurricane intensity and precipitation: Sensitivity to the choice of climate model and convective parameterization. *J. Climate*, **17**, 3477–3495, https://doi.org/10.1175/1520-0442(2004)017<3477:IOCWOS>2.0.CO;2.

——, and Coauthors, 2010: Tropical cyclones and climate change. *Nat. Geosci.*, **3**, 157–163, https://doi.org/10.1038/ngeo779.

——, and Coauthors, 2013: Dynamical downscaling projections of twenty-first-century Atlantic hurricane activity: CMIP3 and CMIP5 model-based scenarios. *J. Climate*, **26**, 6591–6617, https://doi.org/10.1175/JCLI-D-12-00539.1.

Langousis, A., and D. Veneziano, 2009a: Theoretical model of rainfall in tropical cyclones for the assessment of long-term risk. *J. Geophys. Res.*, **114**, D02106, https://doi.org/10.1029/2008JD010080.

——, and ——, 2009b: Long-term rainfall risk from tropical cyclones in coastal areas. *Water Resour. Res.*, **45**, W11430, https://doi.org/10.1029/2008WR007624.

——, ——, and S. Chen, 2008: Boundary layer model for moving tropical cyclones. *Hurricanes and Climate Change*, J. B. Elsner and T. H. Jagger, Eds., Springer, 265–286, https://doi.org/10.1007/978-0-387-09410-6_15.

Large, W. G., and S. Pond, 1981: Open ocean momentum flux measurements in moderate to strong winds. *J. Phys. Oceanogr.*, **11**, 324–336, https://doi.org/10.1175/1520-0485(1981)011<0324:OOMFMI>2.0.CO;2.

Lin, N., and D. Chavas, 2012: On hurricane parametric wind and applications in storm surge modeling. *J. Geophys. Res.*, **117**, D09120, https://doi.org/10.1029/2011JD017126.

——, and K. A. Emanuel, 2016: Grey swan tropical cyclones. *Nat. Climate Change*, **6**, 106–111, https://doi.org/10.1038/nclimate2777.

——, ——, J. A. Smith, and E. Vanmarcke, 2010a: Risk assessment of hurricane storm surge for New York City. *J. Geophys. Res.*, **115**, D18121, https://doi.org/10.1029/2009JD013630.

——, J. A. Smith, G. Villarini, T. P. Marchok, and M. L. Baeck, 2010b: Modeling extreme rainfall, winds, and surge from Hurricane Isabel (2003). *Wea. Forecasting*, **25**, 1342–1361, https://doi.org/10.1175/2010WAF2222349.1.

——, K. Emanuel, M. Oppenheimer, and E. Vanmarcke, 2012: Physically based assessment of hurricane surge threat under climate change. *Nat. Climate Change*, **2**, 462–467, https://doi.org/10.1038/nclimate1389.

Liu, M., and J. A. Smith, 2016: Extreme rainfall from landfalling tropical cyclones in the eastern United States: Hurricane Irene (2011). *J. Hydrometeor.*, **17**, 2883–2904, https://doi.org/10.1175/JHM-D-16-0072.1.

Lonfat, M., 2004: Tropical cyclone rainfall: An observational and numerical study of the structure and governing physical processes. Ph.D. thesis, University of Miami, 135 pp., https://scholarlyrepository.miami.edu/dissertations/2156/.

——, F. D. Marks Jr., and S. S. Chen, 2004: Precipitation distribution in tropical cyclones using the Tropical Rainfall Measuring Mission (TRMM) microwave imager: A global perspective. *Mon. Wea. Rev.*, **132**, 1645–1660, https://doi.org/10.1175/1520-0493(2004)132<1645:PDITCU>2.0.CO;2.

——, R. Rogers, T. Marchok, and F. D. Marks Jr., 2007: A parametric model for predicting hurricane rainfall. *Mon. Wea. Rev.*, **135**, 3086–3097, https://doi.org/10.1175/MWR3433.1.

Lu, P., J. A. Smith, and N. Lin, 2017: Spatial characterization of flood magnitudes over the drainage network of the Delaware River basin. *J. Hydrometeor.*, **18**, 957–976, https://doi.org/10.1175/JHM-D-16-0071.1.

Magagi, R., and A. P. Barros, 2004: Estimation of latent heating of rainfall during the onset of the Indian monsoon using TRMM PR and radiosonde data. *J. Appl. Meteor.*, **43**, 328–349, https://doi.org/10.1175/1520-0450(2004)043<0328:EOLHOR>2.0.CO;2.

Mantilla, R., and V. K. Gupta, 2005: A GIS numerical framework to study the process basis of scaling statistics in river networks. *IEEE Geosci. Remote Sens. Lett.*, **2**, 404–408, https://doi.org/10.1109/LGRS.2005.853571.

Mudd, L., C. Letchford, D. Rosowsky, and F. Lombardo, 2015: A probabilistic hurricane rainfall model and possible climate change implications. *Proc. 14th Int. Conf. on Wind Engineering*, Porto Alegre, Brazil, IAWE, 15 pp., https://doi.org/10.13140/RG.2.1.1971.4401.

Ooyama, K. V., 1969: Numerical simulation of the life cycle of tropical cyclones. *J. Atmos. Sci.*, **26**, 3–40, https://doi.org/10.1175/1520-0469(1969)026<0003:NSOTLC>2.0.CO;2.

Powell, M. D., P. J. Vickery, and T. A. Reinhold, 2003: Reduced drag coefficient for high wind speeds in tropical cyclones. *Nature*, **422**, 279–283, https://doi.org/10.1038/nature01481.

Rappaport, E. N., 2000: Loss of life in the United States associated with recent Atlantic tropical cyclones. *Bull. Amer. Meteor. Soc.*, **81**, 2065–2074, https://doi.org/10.1175/1520-0477(2000)081<2065:LOLITU>2.3.CO;2.

——, 2014: Fatalities in the United States from Atlantic tropical cyclones: New data and interpretation. *Bull. Amer. Meteor. Soc.*, **95**, 341–346, https://doi.org/10.1175/BAMS-D-12-00074.1.

Rasmussen, K. L., S. L. Choi, M. D. Zuluaga, and R. A. Houze Jr., 2013: TRMM precipitation bias in extreme storms in South America. *Geophys. Res. Lett.*, **40**, 3457–3461, https://doi.org/10.1002/grl.50651.

Raymond, D. J., 1992: Nonlinear balance and potential-vorticity thinking at large Rossby number. *Quart. J. Roy. Meteor. Soc.*, **118**, 987–1015, https://doi.org/10.1002/qj.49711850708.

Reinecke, P. A., and D. R. Durran, 2008: Estimating topographic blocking using a Froude number when the static stability is nonuniform. *J. Atmos. Sci.*, **65**, 1035–1048, https://doi.org/10.1175/2007JAS2100.1.

Rezapour, M., and T. E. Baldock, 2014: Classification of hurricane hazards: The importance of rainfall. *Wea. Forecasting*, **29**, 1319–1331, https://doi.org/10.1175/WAF-D-14-00014.1.

Riehl, H., and J. Malkus, 1961: Some aspects of Hurricane Daisy, 1958. *Tellus*, **13**, 181–213, https://doi.org/10.3402/tellusa.v13i2.9495.

Rogers, R., S. Chen, J. Tenerelli, and H. Willoughby, 2003: A numerical study of the impact of vertical shear on the distribution of rainfall in Hurricane Bonnie (1998). *Mon. Wea. Rev.*, **131**, 1577–1599, https://doi.org/10.1175//2546.1.

——, F. Marks, and T. Marchok, 2009: Tropical cyclone rainfall. *Encyclopedia of Hydrological Sciences*, M. G. Anderson and J. J. McDonnell, Eds., Wiley, https://doi.org/10.1002/0470848944.hsa030.

Shapiro, L. J., 1983: The asymmetric boundary layer under a translating hurricane. *J. Atmos. Sci.*, **40**, 1984–1998, https://doi.org/10.1175/1520-0469(1983)040<1984:TABLFU>2.0.CO;2.

Simpson, R. H., and H. Riehl, 1981: *The Hurricane and Its Impact.* Louisiana State University Press, 398 pp.

Smith, J. A., G. Villarini, and M. L. Baeck, 2011: Mixture distributions and the climatology of extreme rainfall and flooding in the eastern United States. *J. Hydrometeor.*, **12**, 294–309, https://doi.org/10.1175/2010JHM1242.1.

Smith, R. B., 2006: Progress on the theory of orographic precipitation. *Tectonics, Climate, and Landscape Evolution*, S. D. Willett et al., Eds., Geological Society of America Special Paper, Vol. 398, Geological Society of America, 1–16, https://doi.org/10.1130/2006.2398(01).

Smith, R. K., 2003: A simple model of the hurricane boundary layer. *Quart. J. Roy. Meteor. Soc.*, **129**, 1007–1027, https://doi.org/10.1256/qj.01.197.

——, and M. T. Montgomery, 2008: Balanced boundary layers used in hurricane models. *Quart. J. Roy. Meteor. Soc.*, **134**, 1385–1395, https://doi.org/10.1002/qj.296.

——, and ——, 2010: Hurricane boundary-layer theory. *Quart. J. Roy. Meteor. Soc.*, **136**, 1665–1670, https://doi.org/10.1002/qj.679.

Tuleya, R. E., M. DeMaria, and R. J. Kuligowski, 2007: Evaluation of GFDL and simple statistical model of rainfall for U.S. landfalling tropical storms. *Wea. Forecasting*, **22**, 56–70, https://doi.org/10.1175/WAF972.1.

Ueno, M., 2007: Observational analysis and numerical evaluation of the effects of vertical wind shear on the rainfall asymmetry in the typhoon inner-core region. *J. Meteor. Soc. Japan*, **85**, 115–136, https://doi.org/10.2151/jmsj.85.115.

Vickery, P. J., F. J. Masters, M. D. Powell, and D. Wadhera, 2009: Hurricane hazard modeling: The past, present, and future. *J. Wind Eng. Ind. Aerodyn.*, **97**, 392–405, https://doi.org/10.1016/j.jweia.2009.05.005.

Villarini, G., and J. A. Smith, 2010: Flood peak distributions for the eastern United States. *Water Resour. Res.*, **46**, W06504, https://doi.org/10.1029/2009WR008395.

——, D. A. Lavers, E. Scoccimarro, M. Zhao, M. F. Wehner, G. A. Vecchi, T. R. Knutson, and K. A. Reed, 2014a: Sensitivity of tropical cyclone rainfall to idealized global-scale forcings. *J. Climate*, **27**, 4622–4641, https://doi.org/10.1175/JCLI-D-13-00780.1.

——, R. Goska, J. A. Smith, and G. A. Vecchi, 2014b: North Atlantic tropical cyclones and U.S. flooding. *Bull. Amer. Meteor. Soc.*, **95**, 1381–1388, https://doi.org/10.1175/BAMS-D-13-00060.1.

Wilson, P. S., and R. Toumi, 2005: A fundamental probability distribution for heavy rainfall. *Geophys. Res. Lett.*, **32**, L14812, https://doi.org/10.1029/2005GL022465.

Wingo, M. T., and D. J. Cecil, 2010: Effects of vertical wind shear on tropical cyclone precipitation. *Mon. Wea. Rev.*, **138**, 645–662, https://doi.org/10.1175/2009MWR2921.1.

Wong, M. L. M., and J. C. L. Chan, 2004: Tropical cyclone intensity in vertical wind shear. *J. Atmos. Sci.*, **61**, 1859–1876, https://doi.org/10.1175/1520-0469(2004)061<1859:TCIIVW>2.0.CO;2.

Wright, D., T. Knutson, and J. Smith, 2015: Regional climate model projections of rainfall from U.S. landfalling tropical cyclones. *Climate Dyn.*, **45**, 3365–3379, https://doi.org/10.1007/s00382-015-2544-y.

Yang, M. J., S. A. Braun, and D. S. Chen, 2011: Water budget of Typhoon Nari (2001). *Mon. Wea. Rev.*, **139**, 3809–3828, https://doi.org/10.1175/MWR-D-10-05090.1.

Zhu, L., S. M. Quiring, and K. A. Emanuel, 2013: Estimating tropical cyclone precipitation risk in Texas. *Geophys. Res. Lett.*, **40**, 6225–6230, https://doi.org/10.1002/2013GL058284.